
# University of Padova

Department of Information Engineering

*Master Thesis in Electronic engineering*


# DESIGN OF SWEPT SOURCE OPTICAL COHERENCE TOMOGRAPH


*Supervisor*
Prof. Luca Palmieri
University of Padova

*Master Candidate*
Mattia Franchin

*Student ID*
2028988


*Academic Year*
2022-2023

23th October, 2023

"Ciò che conosciamo di noi è solamente una parte, e forse piccolissima, di ciò che siamo a nostra insaputa."
— Luigi Pirandello

# Abstract

Optical coherence tomography (OCT) is a non-invasive medical imaging technique that plays a crucial role in ophthalmological diagnostics and a growing variety of medical applications. In particular, the Swept Source OCT (SS-OCT) device represents one of the most recent evolutions in the OCT field, offering greater acquisition speed and greater penetration depth compared to OCTs based on traditional spectrometry or interferometry in the time.

This master thesis focuses on the optimization of a customized SS-OCT device for advanced medical applications. The design is based on a swept laser source, which offers a range of optical wavelengths with high spectral resolution and a high scanning frequency.

The primary goal of this research was to develop an SS-OCT system capable of providing images with high resolution and sufficient penetration depth to visualize microstructural details in biological tissues, while enabling rapid image acquisition. One of the major problems relating to the loss of axial resolution, i.e. the chromatic dispersion that occurs inside the interferometer, has also been reported. The design steps were supported by computational simulations and experimental tests.

Future evolutions of the setup could concern a further improvement of the axial resolution, further decreasing the phase difference between the two branches of the interferometer on which the entire device is based and introduced by the chromatic dispersion, and the implementation of more advanced technologies such as polarization-sensitive OCT (PS-OCT).

# Sommario

La tomografia a coerenza ottica (OCT) è una tecnica di imaging medico non invasiva che svolge un ruolo cruciale nella diagnostica oftalmologica e in una crescente varietà di applicazioni mediche. In particolare, il dispositivo Swept Source OCT (SS-OCT) rappresenta una delle più recenti evoluzioni nel campo degli OCT, offrendo maggiore velocità di acquisizione e maggiore profondità di penetrazione rispetto agli OCT basati sul dominio temporale e sulla tradizionale spettrometria o interferometria.

Questa tesi si concentra sull'ottimizzazione di un dispositivo SS-OCT per applicazioni mediche avanzate. Il progetto si basa su una sorgente laser a scansione, che offre una gamma di lunghezze d'onda ottiche con elevata risoluzione spettrale e un'elevata frequenza di scansione.

L'obiettivo principale di questa ricerca era quello di sviluppare un sistema SS-OCT in grado di fornire immagini ad alta risoluzione e profondità di penetrazione sufficiente per visualizzare i dettagli microstrutturali nei tessuti biologici, consentendo al contempo una rapida acquisizione delle immagini. È stato analizzato anche uno dei maggiori problemi relativi alla perdita di risoluzione assiale, ovvero la dispersione cromatica. Le fasi di progettazione sono state supportate da simulazioni computazionali e prove sperimentali.

Future evoluzioni del setup potrebbero riguardare un ulteriore miglioramento della risoluzione assiale, diminuendo ulteriormente la differenza di fase tra i due rami dell'interferometro su cui si basa l'intero dispositivo e introdotta dalla dispersione cromatica, e l'implementazione di tecnologie più avanzate come l'OCT sensibile alla polarizzazione (PS-OCT).

# Contents

# Listing of figures

# Listing of tables

# Listing of acronyms

**BPD** . . . . . Balanced photodiode

**DAQ** . . . . . Data Acquisition

**DOF** . . . . . Depth Of Focus

**FDOCT** . . . . . Fourier Domain OCT

**FFT** . . . . . Fast Fourier Transform

**FOV** . . . . . Field Of View

**FWHM** . . . . . Full Width Half Maximum

**MZI** . . . . . Mach-Zehnder Interferometer

**OCT** . . . . . Optical Coherence Tomography

**PSD** . . . . . Power Spectral Density

**RNFL** . . . . . Retinal Nerve Fiber Layer

**SDOCT** . . . . . Spectral Domain OCT

**SMF** . . . . . Single Mode Fiber

**SNR** . . . . . Signal to Noise Ratio

**SSOCT** . . . . . Swept Source OCT

**TDOCT** . . . . . Time Domain OCT

**TEM** . . . . . Transverse Electric and Magnetic

**VOA** . . . . . Variable Optical Attenuator

# 1 Introduction

## 1.1 Advantages of optical imaging

Optical imaging uses light to study cellular and molecular functions in living organisms as well as animal and plant tissues. Information is ultimately derived from tissue components and biomolecular processes. One of the most important advantages of using optical imaging is to limit the patient's exposure to dangerous radiation by using non-ionizant radiation, which includes visible, ultraviolet, and infrared light. Thank to the use of safe radiation, optical imaging can be used for repeated analysis to follow the evolution of the diseases or the progress of the treatment. Typically, medicine applications of the optical imaging regard soft tissues because thanks to its sensitivity to the wide variety of ways in which soft tissues can absorb or scatter the light, it can detect metabolic changes that are early markers of disease. Of course, optical imaging can be also combined with ultrasound images or images detected with ionizing radiation in order to provide enhanced information for monitoring more complex diseases. [15] [16] The study conducted in this thesis regards one of most fast growing imaging technology of the last decades: the Optical Coherence Tomography (OCT).

## 1.2 Basic concepts on OCT

OCT is a three-dimensional imaging technique based on the measurements of the reflected light from the tissue discontinuities, which can achieve high spatial resolution and large penetration depth. Since it is a non-contact imaging, it's particularly valuable in organs such as the eyes, where the traditional diagnosis through means of biopsy is not available. [15] It employs light from a broadband light source, which is divided into a sample and a reference beam thank to an optical splitter,then the light wave scattered from the sample interferes with the reference beam, creating a interference pattern which is useful in order to measure the light echoes versus the depth profile of the tissue. [17] The TD-OCT has been the first technology introduced to the market and it requires acquisition of a depth scan at multiple location, so the scan speed and the quality images are very poor. The introduction of the SD-OCT overcomes these problems since the scan is performed all over the organ simultaneously. Indeed, as highlighted in Fig.1.1a, time domain OCT suffers of a lower SNR than the one of the spectral domain OCT (Fig.1.1b), so that SD-OCT has become the main solution for most applications.

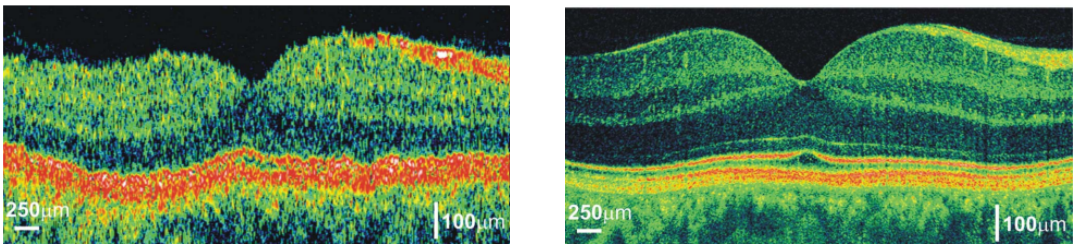


**(a)** time domain detection **(b)** spectral domain detection

**Figure 1.1:** Comparison of OCT cross-sectional imaging of the human eye in vivo [1]

The main characteristics of TD-OCT and SD-OCT will be discuss in Cap.2

## 1.3 Applications in medicine

Novel medical imaging technologies can enhance the diagnosis and clinical management of diseases and contribute to a better understanding of disease pathogenesis, thus aiding the development of novel therapies. Consequently, imaging technologies have a significant impact on medical research and clinical practice. Three of the possible applications of an OCT device will be presented below: the first concerns the ophthalmological field, the field in which OCT was born; then the application in dermatology will be illustrated, a field in which OCT is gradually

finding more and more application and finally a particular application will be illustrated where the optical head must be resized and inserted into a catheter for intra-coronary examinations.

### 1.3.1 Ophthalmology

The human eye is fundamentally transparent, allowing the passage of light with minimal optical attenuation and scattering, facilitating easy optical access to both the anterior segment and the retina. As a result, ophthalmic imaging, especially retinal imaging, has been the first but also the most successful clinical application of optical coherence tomography (OCT). This technology has significantly enhanced the potential for early retinal diseases diagnosis,because of it's make more clear their genesis, and their recovery monitoring of their progression and response to therapies. Thanks to ultrabroad bandwidth light sources and high-speed detection techniques, high quality results were achieved for performing noninvasive optical biopsies of the living human retina. Furthermore, development in axial resolution and speed allow the three-dimensional rendering of retinal volumes and also high-definition two-dimensional tomograms, topographic thickness maps of intra-retinal layers,but also a volumetric quantification of pathological intra-retinal changes. The development of light sources emitting wavelength around $1050nm$, has enabled three-dimensional OCT imaging with enhanced choroidal visualization but, thank to the fact that in this wavelength region there are reduced scattering losses , has also improved OCT performance in cataract patients. Since it birth, OCT was conceived as a non-invasive imaging method of the eye, therefore without excision, with a resolution approaching that of histology. A big step in this direction was made when it was possible to reach a resolution around 10 micrometres and subsequently in the submicrometric order of magnitude, managing to view even the intra-retinal layers. Today is possible to see also photoreceptor layer impairment in macular pathologies, retinitis pigmentosa or the age-related macular degeneration.

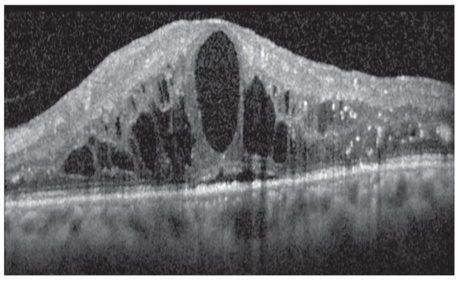

**Figure 1.2:** Example of disease saw with OCT: macular edema. It's caused by the leakage of blood from the capillaries of the macula, i.e. the central part of the retina[2]

The development of OCT systems which operate with wavelength longer than $1310nm$ was a crucial step to have an imaging device able to get corneal and anterior segment images. As reported in Fig.1.3, a $1310nm$ wavelength is strongly absorbed by water within the path from cornea to the retina, limiting a lot the exposure. Conversely, the use of a shorter wavelength ($830nm$ for example) means that an high amount of light reaches the retina, endangering the patient's health. This means that, working with longer wavelengths, it's possible to use more power, speeding up the scan speed without sacrificing signal level. Another important advantage of using longer wavelengths derives from the fact that OCT systems generally had poor capabilities of getting high quality images in opaque tissue due to signal attenuation by scattering. Therefore, considering that scattering level is inversely proportional to the wavelength, using $1310nm$ wavelength gives much more possibilities to penetrate the tissue. Seeing Fig.1.4) it's possible to notice that systems which work with longer wavelength (such as $1310nm$) can highlight details like scleral spur and angle recess, impossible to see with $830nm$ wavelength devices.[3]

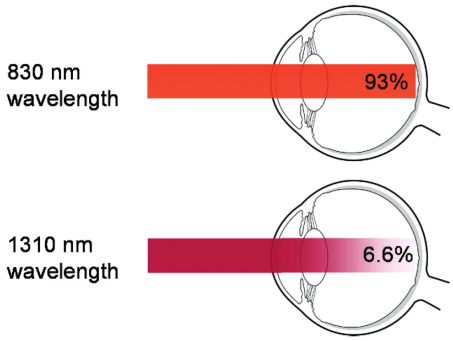


**Figure 1.3:** Attenuation of light in a single pass from cornea to retina[3]

**Figure 1.4:** A comparison of the same portion of the anterior chamber took at $830nm$ on the left and at $1310nm$ on the right[3]

### 1.3.2 Dermatology

Dermatology is one of the branches of medicine that has mostly used, and still uses today, histological examinations after an excision. However, approaches of this type has severe disadvantages, such as artifacts of the tissue like dehydration, shrinkage and collapse of vessels. Moreover, the preparation of the probe could be expensive and it can require a lot of time and in general, this type of exam is not repeatable because it just provides a snapshot of the health of the tissue. For these reasons, it's clear how a non invasive and in-vivo imaging technique can improve dermatology exams. OCT fits into this context, which is able to provide dynamic images with a resolution of $15\mu m$ and less of the various tissues, shortening times and reducing costs. The major problem of applying an optical imaging technique in the dermatology field is that the skin is a strong medium of dispersion, so the image depth is limited. Anyhow, it's possible to see the structure of the skin with also blood vessels, hair follicles and glands.

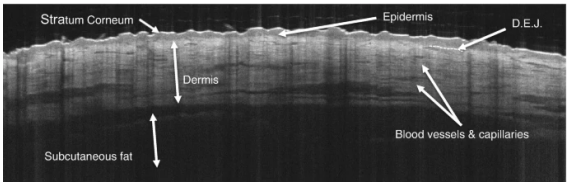


**Figure 1.5:** OCT scan of healthy skin (D.E.J.= dermal-epidermal junction)[4]

The visible appearance of normal healthy skin depends on its position. Normally, due to an high difference in refractive indexes between high and skin, there's and high reflection of light, which cause an high entrance signal and it can be smoothed by the application of gel on the skin surface. As reported in Fig.1.5, this layer is called stratum corneum, which is about $10\mu m$ thick. Going deeper, there's the epidermal layer, in which dispersion is low and homogeneous. Then, beyond the D.E.J., there's the papillary dermis, characterized by an high signal intensity due to an irregular distribution of capillaries and collages bundles. Unfortunately, in deeper parts of the dermis, multiple scattering and absorption phenomena come into play degrading the signal strength.
OCT devices are able to detect all the three types of skin tumor:

- Epithelial tumors likes basal cell carcinomas, whose cell aggregates emits similar signal in density and distribution compared to the epithelium, but they are characterized by enlarged blood vessel next to them. It's more complicated to see squamous cell carcinomas instead, because of the stronger keratinization of the tumor, and it's possible to detect the lateral and the lower margins only with small aggregates;

- Mesenchymal tumors like fibrous histiocytoma in which the signal intensity can be stronger or lower compared to the adjacent dermis;
- Melanocytic tumors are strong scattering areas, which return cloudy images. This happens because melanin pigment increases the signal attenuation coefficient and the scattering. OCT systems can also distinguish between benign and malignant melanocytic nevi thank to a less homogeneous signal distribution in the second ones.

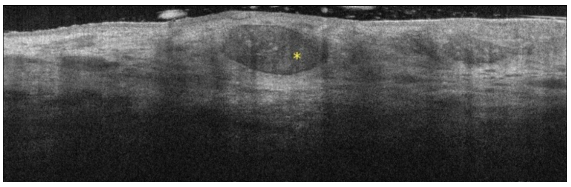

**Figure 1.6:** Example of an OCT image that shows nodular basal cell carcinoma (BCC) with a basal nest centrally (star) [5].

### 1.3.3 Cardiology

Even though OCT has a useful high resolution, its application in cardiology, especially in the intra-coronary context has thus far been limited.The major difficulty of intra-coronary OCT is due to the presence of blood, which must necessarily be removed from the imaging field in order to examine the artery walls. The most common methods to resolve this problem are based on coronary artery lavage with saline solution at the exam site to be done with or without proximal balloon occlusion. Although analyzes and studies have been carried out to improve these procedures, they still remain a source of risk of myocardial ischemia during the examination, which represents a highly limiting factor for the application of this technology. Fortunately, with the improvement of technology and the advent of FD-OCT, the average duration of an exam has dropped dramatically and with it the likelihood of endangering the patient's health. In the field of cardiology, OCT is mainly used for:

- Percutaneous coronary intervention(PCI) guide and optimisation.
- Evaluation of stent coverage and positioning, and verification of stent restenosis;
- Atherosclerotic plaque assessment;

A brief description of the three applications follows.
PCI has become the most used treatment of ischemic heart disease due to obstructive coronary artery disease both in the context of stable angina and in acute coronary syndromes and has

drastically reduced mortality from ischemic heart disease. In this particular treatment, OCT is mainly used in two phases. The first phase involves the study of the pathological section of the artery, the measurement of the diameter of the lumen, the characterization of the culprit lesion, and the possible presence of other vulnerable plaques at risk of rupture. Furthermore, in the context of bifurcation lesions, it can provide important information regarding the status of the lateral branch, providing a clearer vision and helping in the decision to adopt the most appropriate technique.The second phase, following the PCI, concerns the evaluation of the result of the operation and its possible complications. OCT can provide important information, such as luminal diameters and area of the stented coronary segment, which correlate with the risk of restenosis. Furthermore, it is able to reveal incomplete coverage of the atherosclerotic lesion and therefore the need for a second stent, or the state of a segment in which multiple stents overlap. The high resolution of OCT is very helpful also to predict stent thrombosis. Indeed OCT analysis regard the concerns the state of neo-intimal coverage of the stent over time, which is a powerful predictor of thrombosis, as it has been established that non-optimal coverage is very likely to cause such problems.(Fig.1.8)

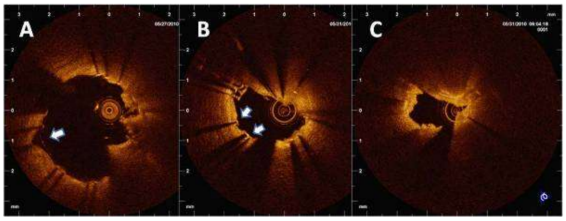


**Figure 1.7:** Example of late stent thrombosis. A: Thrombus at a proximal edge of the stent. Bad positioned and uncovered struts(White arrow). B: Cross section of subocclusion with bad positioned struts (arrows). C: cross section at level of the thrombotic[6]

One of the most common causes of acute coronary syndromes is the rupture of the atherosclerotic plaque with consequent thrombosis.Fortunately, thanks to a high resolution imaging system such as OCT, it is possible to recognize vulnerable plaques by analyzing their morphology and composition. Thanks to studies also carried out with OCT it was possible to recognize the most vulnerable plaques: they present a fibrous cap with inflammation and activated macrophages in the vicinity. The presence of these anti-inflammatory cells greatly increases the probability of breaking the fibrous cap, as once active they release a protein, metalloproteinases, which is associated with a greater ability to cause this cap to detach.(Fig1.8)

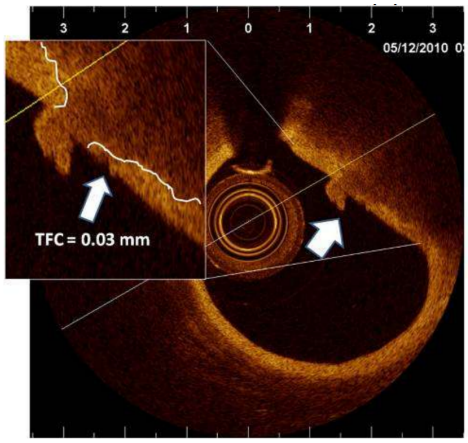


**Figure 1.8:** Vulnerable plaque with a thin fibrous cap(TFC). White lines highlights the interface between lipid pool and the fibrous cap.[6]

## 1.4 Thesis structure

The study conducted in this thesis had the objective of optimizing a SS-OCT system using as starting point the previous thesis ([18],[19]) developed in Photonic and Electromagnetic Group Laboratory at the Department of Information Engineering of the University of Padova. In particular the theoretical principles useful for designing an OCT system, the parts that make up this device, the resolution of common problems and its operation will be discussed.

# 2

# OCT principles

## 2.1 Light as electromagnetic wave phenomenon

The principles behind optical imaging techniques are strictly related to the behaviour and the characteristics of light, and they are essential for understanding the factors to consider for devices design. In order to understand this thesis, knowledge of the double nature of light is assumed. Indeed, according to the wave theory, light is an electromagnetic wave phenomenon which propagates, in vacuum, with a speed equal to $c \approx 3 \times 10^8 m/s$, meanwhile, every other homogeneous medium of propagation is has its own refractive index $n$, which slows down the wave propagation to $v_p = c/n$. While the wave theory explains propagation, the processes of generation, absorption or scattering can be explained by quantum or particle theory, which describes light as a transfer of energy by particles called photons. In order not to weigh down this discussion more than necessary, the most important characteristics of the first theory will be illustrated.

As already said, light is a electromagnetic radiation, which means it propagates through magnetic and electric transverse fields. Taking into account a monochromatic light, it can be expressed according to the vector equations

$$\vec{E}(z,t) = E_0 \cos(kt - \omega z + \varphi)\hat{a}_1 \tag{2.1}$$

$$\vec{B}(z,t) = B_0 \cos(kt - \omega z + \varphi)\hat{a_2} = \frac{1}{c} E_0 \cos(kt - \omega z + \varphi)\hat{a_2} \tag{2.2}$$

where $a_1$ and $a_2$ are directions perpendicular to each other and perpendicular to the direction of propagation of the wave as illustrated in fig.2.1

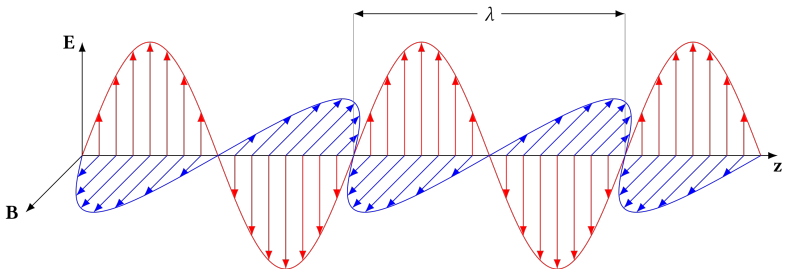


**Figure 2.1:** Electromagnetic wave propagation

Hence,once the amplitude of the electric field and the polarization direction are known, there are information hidden regarding the magnetic field. For this reason, from now on, only electric plane wave of monochromatic light is taken into consideration.

### 2.1.1 Polarization

Considering a forward moving along z wave and letting be $\vec{E_0} = \hat{x}A_x e^{i\varphi_x} + \hat{y}A_y e^{i\varphi_y}$, the electric field can written as

$$\vec{E}(z) = (\hat{x}A_x e^{i\varphi x} + \hat{y}A_y e^{i\varphi y}) e^{ikz} \tag{2.3}$$

or in time domain

$$\vec{E}(z,t) = Re\left[\vec{E}(z)e^{-i\omega t}\right] = \begin{pmatrix} A_x \cos(kz - \omega t + \varphi_x) \\ Ay \cos(kz - \omega t + \varphi_y) \\ 0 \end{pmatrix} \tag{2.4}$$

which allows to get the instantaneous amplitude and direction of $\vec{E}(z,t)$. Depending on the ratio $A_y/A_x$ and the phase difference $\varphi_y - \varphi_x$ there are three types of polarization:

- Linear polarization with $\varphi_y - \varphi_x = 0, \pi$;
- Circular polarization with $\varphi_y - \varphi_x = \pm\pi/2$ for right-handed and left-handed polarization,respectively and $A_x = A_y = A$;

- Elliptical polarization with $\varphi_y - \varphi_x \neq 0, \pi$, $\varphi_y - \varphi_x > 0$ for right handed polarization and $\varphi_y - \varphi_x < 0$ for left-handed polarization, and $A_x \neq A_y$.

One of the main aspects of polarization in the OCT field, is that weak asymmetries and non-uniform stresses to which the core of the optical fiber is subjected cause a local variation of the refractive index, making the medium birefringent. A varying birefringence along the fiber will cause each polarization mode to travel at different velocity. This phenomenon is called *polarization-mode dispersion (PMD)* and the difference in propagation time $\Delta\tau_{PMD}$ between two orthogonal polarization states causes spread of the pulse, degrading the image quality (see Fig.2.2. [20]

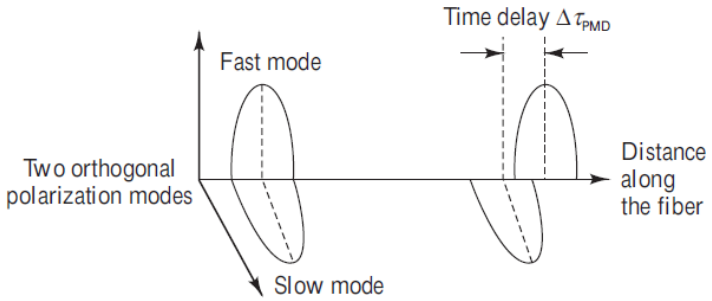


**Figure 2.2:** Polarization Mode Dispersion

As reported in Sec.2.4.3, a control of the polarization states into the OCT device is extremely important, because it can make the difference between a good and a poor quality image. The polarization controller used in the project uses in turn the birefringence to balance the mismatch between the two arms.

## 2.1.2 Coherence, Interference and beat frequency

### 2.1.2.1 Coherence

Coherence is one of the key points in OCT system design, because it influences the entire mathematical treatment and therefore the predictability of the results. A light field is called coherent when there's a fixed phase relationship between the electric field values at different locations or at different times. In a more practicable way,it can be defined the time coherence $t_c$ as the temporal interval over which the phase of a light wave can be predicted accurately at a given point in space (Fig.2.3). If $t_c$ is large, that light has an high degree of coherence, instead a small $t_c$ describes a low coherent light. A perfect coherent light has the maximum degree of coherence

(equal to 1) and it can be emitted by a monochromatic source, and it will be a sinusoidal wave with a predictable phase. Instead in complex system such as a SS-OCT, the light sources emit a low-coherence light because they are broadband. The corresponding spatial interval $l_c = c \cdot t_c$ is called coherence length and it represents the path length that a photon travels during the coherence time.

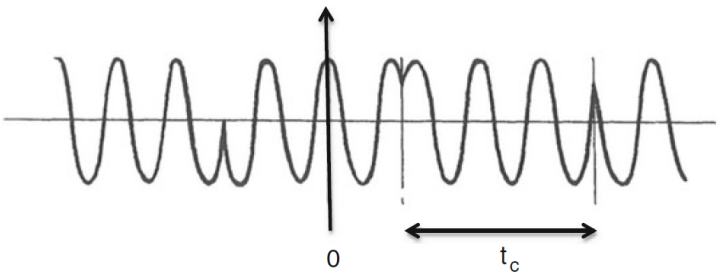


**Figure 2.3:** Coherence time in a random infinite sinusoid

#### 2.1.2.2 Interference

Coherence is strongly related to the ability of light to exhibit interference effects. Let's consider, for simplicity, only two monochromatic plane waves, which produce the following electric field in a certain point of the space:

$$\vec{E} = \vec{E_1} + \vec{E_2} = |\vec{E_1}|e^{j\left(\vec{kr}-\omega t+\varphi_1\right)} + |\vec{E_2}|e^{j\left(\vec{kr}-\omega t+\varphi_2\right)} \tag{2.5}$$

which means, in terms of light intensity:

$$I = \frac{1}{2}\varepsilon_0 c|\vec{E_1}|^2 + \frac{1}{2}\varepsilon_0 c|\vec{E_2}|^2 + \varepsilon_0 c|\vec{E_2}^*\vec{E_1}|\cos\left(\varphi_1 - \varphi_2\right) \tag{2.6}$$

known as the interference equation and it shows that the intensity of the composite light wave depends not only on the intensity of each light wave, but also on the pahse difference between the two waves. In particular the last term is called interference term and it reveals if there's a constructive ($\delta\varphi = 2n\pi$) or a destructive ($\delta\varphi = (2n+1)\pi$) interference between waves whenever the phase difference is constant, instead if it fluctuates in time the two waves are partially coherent.

### 2.1.2.3 Interferometers

Interferometry, which analyzes interference effects between waves, is based on interferometers. The most simple one is the Michelson interferometer, whose schematic diagram is reported in Fig.2.4. A laser source emits a coherent electric field $\vec{E}$, which is splitted into two electric field, $\vec{E_1}$ and $\vec{E_2}$ by a 50:50 beam splitter. $\vec{E_1}$ is sent to a fixed mirror, instead $\vec{E_2}$ goes to a moving mirror. Once they are scattered back from their respective mirrors, they are recombined and sent to the detector. The two fields arrive at the detector with a time difference given by

$$\tau = 2\frac{L_1 - L_2}{c} \tag{2.7}$$

where c is the speed velocity in the medium, and $L_1 - L_2$ is the difference path length between each mirror and the splitter, traveled twice. From eq.2.6, considering that $I = I_1 = I_2$, it results that the light intensity measured by the detector is:

$$I_{meas} = I + I + 2IRe\left[e^{2ik(L_1 - L_2)}\right] = 2I\left\{1 + \cos\left(2\pi\frac{\Delta L}{\lambda}\right)\right\} \tag{2.8}$$

with $\Delta L = L_1 - L_2$

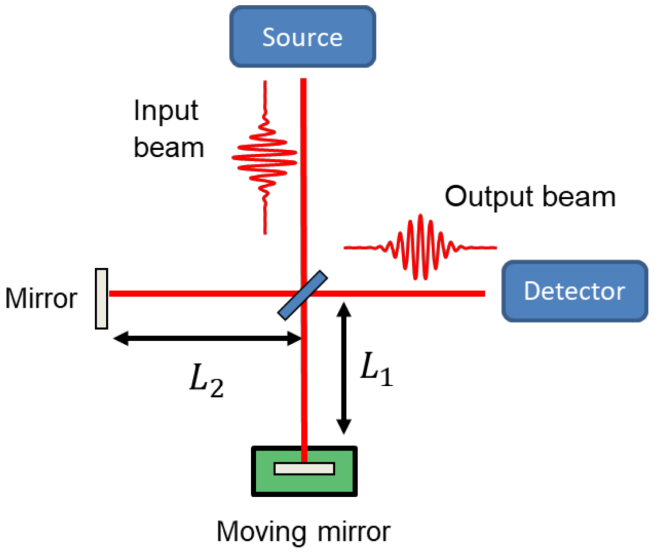


**Figure 2.4:** Michelson interferometer

Whenever laser source emits an ideal coherent light wave, scanning the path length $\Delta L$ the Michelson interferometer measures the wavelength, because the signal detects is a sinusoid as

function of $\Delta L$, where fringes have a period equal to $\lambda$. Thus, due to the periodic result, a monochromatic laser source is not indicated to measure the depth of the echos of the moving mirror. Instead, if a broadband (and so a low coherence) laser source is used, constructive interference is only observed when the path lengths of the two arms are matched to within the coherence length of the light (Fig.2.5)

In particular, the light intensity that arrives at the detector is:

$$I_{out}(t) \propto |E(t) + E(t-\tau)|^2 = |E(t)|^2 + |E(t-\tau)|^2 + 2Re\left[E(t)E^*(t-\tau)\right] \tag{2.9}$$

but the one measure by the detector over a long time T is:

$$I_{meas} \approx \lim_{T\to\infty} \frac{1}{T} \int_{-T//2}^{T//2} I_{out}(t)\, dt \tag{2.10}$$

so the intensity measured is:

$$I_{meas} \approx 2I_{in} + c\varepsilon_0 Re\left[\langle E(t)E^*(t+\tau)\rangle\right] \tag{2.11}$$

where $I_{in}$ is the mean intensity of the source. From eq.2.11, if the relative delay before the two arms is much larger than the coherence time, so $\tau >> \tau_c$, the last terms goes to zero and $I_{meas} \approx 2I_{in}$, in the other hand, if $\tau \to 0$, $I_{meas}$ is approximately equal to $4I_{in}$. So whenever the interferometer is balanced the interferometer effectively measures the field autocorrelation of the light, meanwhile the echo time and the magnitude are the results of scanning the reference arm, once the interference signal is demodulated.

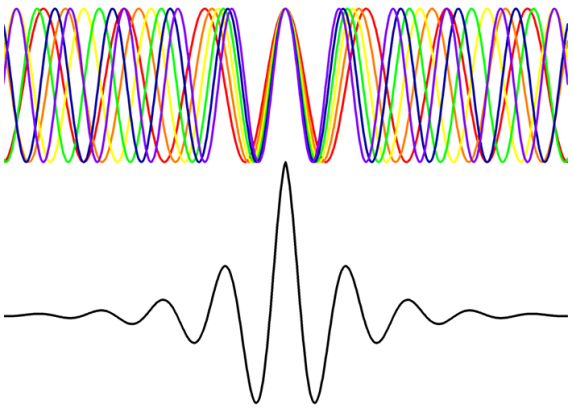

**Figure 2.5:** Example of low coherent light interferometer: constructive interference occurs only when $\Delta L < l_c$

#### 2.1.2.4 Beat frequency

The last important concept about the electromagnetic waves for this project regards the interaction between two electromagnetic waves: it's the beat frequency. This happens whenever two waves with slightly different frequencies overlap and the result is a new waves that seems to "beat" or to oscillate with a lower frequency. This frequency is called beat frequency and it's the difference between the frequencies of the two original waves. To make more clear this phenomena, let's consider two waves, the first with a 15MHz frequency, the second set at 14MHz. As soon as they are summed, the resulting wave has a frequency of 1MHZ, as expected (See Fig.2.6 ).

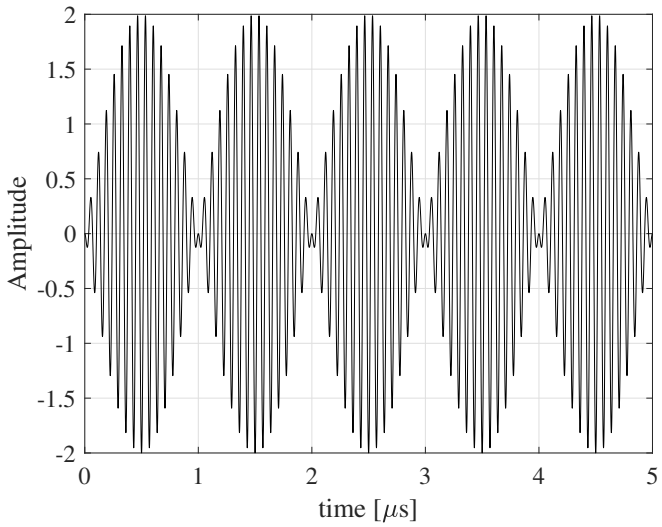


**Figure 2.6:** Example of beat signal due to two sinusoids with frequency equal to 14MHz and 15MHz

## 2.2 Time domain OCT

The first OCT device in literature was a time domain OCT device[7]. It is based on a Michelson interferometer (Fig.2.7) which performs low-coherence reflectometry, because, as highlighted in Sec.2.1.2.3, it can be applied by using continuous wave light instead of ultrashort pulse laser sources. In particular, the OCT scanner in time domain OCT is an extension of the Michelson interferometer, in which an high speed and continuous motion longitudinal scanning is performed in order to have a quite high data acquisition rate. Once the interferometric modulation is detected by the photodetector, the signal is demodulated to produce the envelope of

the interferometric signal and then it's digitized in order to be stored on computer.

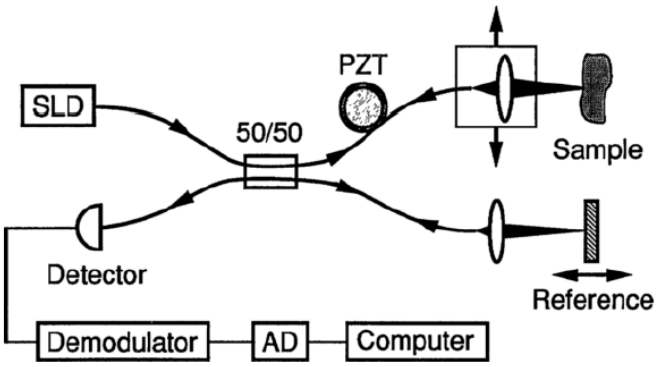


**Figure 2.7:** Diagram of the basic TD-OCT setup using a Michelson interferometer used in [7]

Calling the *sample arm* and *reference arm* respectively the arms of the interferometer with the moving mirror and the sample, the total field made up of the superposition of the echoes coming from the sample can be written as:

$$E_S(t) = \int_0^L \rho_m E(t - 2\tau_m)\, dz \tag{2.12}$$

where $\rho_m$ is the complex amplitude of the echoes, E(t) is the light coming from the source and $\tau_m = {}^{z_m}/_{c}$ is the delay of the propagation up to the sample point located at $z_m$ within the interval $[0, L]$, which is the extension of the sample.

So the total field as the sum of one coming from both the arms is

$$E_{tot}(t) = E(t - 2\tau_R) + E_S(t) \tag{2.13}$$

where $\tau_R$ is the delay of the reference arm. Thus, considering $L_R$ ad the position of the mirror, the mean intensity measured is

$$I_{meas} = \langle I(t) \rangle \propto I_R + I_S + 2Re\left[\int_0^L \rho(z)\Gamma\left(\frac{2}{c}(z - L_R)\right) dz\right] \tag{2.14}$$

which means the detector effectively measures the convolution between the tissue profile and the autocorrelation function $\Gamma(\tau)$ of the source. This means that, scanning the entire sample, the light beam reflected by the mirror located in the position $z_i$ in the reference arm interferes with all the reflection in the sample at a depth $z \in [z_i - l_c/2, z_i + l_c/2]$. Thus, the coherence length $l_c$ determines the width of the peak interference signal. Normally,it desiderable to have

a low broadness of the interference signal, which means to have a well-defined location of the backscattering point. This can be achievied using a low coherence light source, which emits a broad spectral bandwidth. Commonly, a source with Gaussian PSD is used, so that the coherence length it's equal to the full width half maximum (FWHM) of the envelope:

$$l_c = \frac{2\ln 2}{\pi}\frac{\lambda_0^2}{\Delta\lambda} \tag{2.15}$$

where $\lambda_0$ is the central wavelength of the gaussian profile and $\Delta\lambda$ is the bandwidth corresponding to the FWHM level.

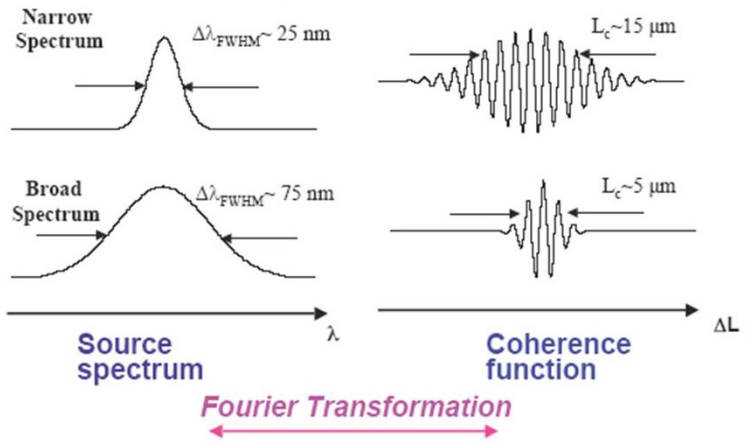


**Figure 2.8:** Relationship between FWHM of a Gaussian PSD and the coherence length

## 2.3 Fourier domain OCT

Beyond time detection, it is also possible to work in the Fourier domain by measuring the interference spectrum. The first example of this approach in literature dates back to 1995[21]. Essentially, there are two types of Fourier detection:

- Spectral domain OCT, based on an interferometer with a spectrometer as a detector;
- Swept Source OCT, in which detectors measure interference signal as a function of time for a frequency-swept light source.

### 2.3.1 Spectral domain OCT

In the spectral domain OCT, the photo detector is substituted by a spectrometer, made up of a diffraction grating that disperses the spectrum of the signal and an array of photodiodes or a line camera, which effectively detect the spectrum. As shown in Fig.2.9, in this configuration the reference arm doesn't moved, but it is fixed, so the path length difference between the two arms is constant. Measuring the interference fringes in the k-space gives a more complete view of the entire interferogram, not just the ones at equal path length, so it allows to detect information about depth sample in a more efficient way. Indeed, keeping in mind that $k = \frac{2\pi}{\lambda}$, eq.2.14 can be rewritten as:

$$I_{meas}(k) \propto I(k) \cos(k\Delta z) \tag{2.16}$$

where $I(k)$ is the field intensity coming from the source and $\Delta z$ is the path length difference between the $i_{th}$ reflector and the reference arm. So, there is no more dependence on the relative position between the mirror of the reference arm and the sample, but now the measure depends on $k$. This means that the interference of two beams have a spectral modulation as function of frequency, measured by a spectrometer. Different echo delays produce different frequency modulations, so they can be measured by rescaling from wavelength to frequency the spectrometer output and then calculate the Fourier transform of the interference signal. So it's possible to obtain the magnitude and echo delay of the light signal which comes from the tissue, having an axial scan measurement.

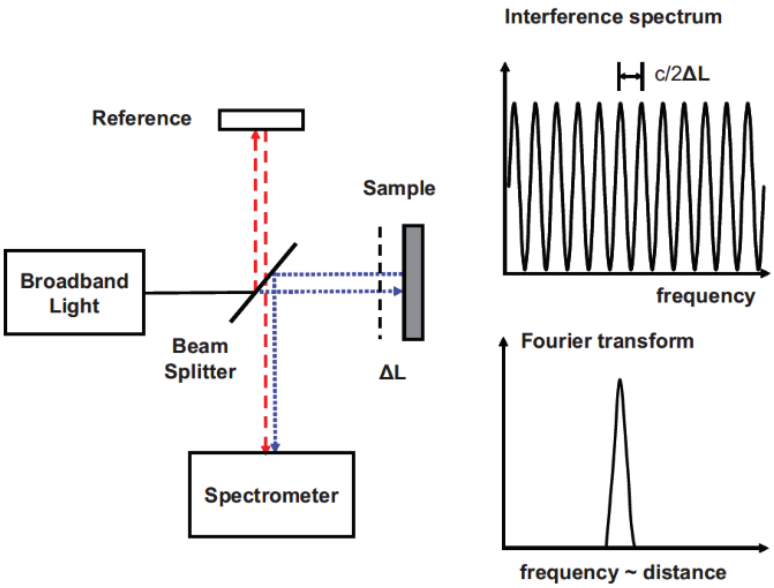


**Figure 2.9:** Diagram of a SD-OCT device.[3]

### 2.3.2 Swept Source OCT

A more complete discussion is reserved for the technology on which this thesis is based: the SS-OCT. It uses an interferometer, in this particular work an Mach-Zehnder interferometer, and a light source which is swept in frequency over time. This change in frequency is used as a label of the different time delays in the light beam, which is detected by interference and Fourier transforming. As shown in Fig.2.10, the signal and the reference light have a time delay determined by the difference of the path length the two arms, related to the depth of the structure in the tissue. Since the light source sweeps the frequency as a function of time, the light echoes coming from the sample have a frequency offset from the signal of the reference arm. As soon as the sample signal and the reference signal interfere, a beat signal is produced at a frequency given by the offset that exists between the beams of the arms. Thus, different echo delays produce different frequency modulations. Ideally, a swept-source laser for SS-OCT should have a linear frequency sweep that it could be written as:

$$f(t) = f_0 + \sigma_f t \tag{2.17}$$

where $f_0$ is the starting frequency $\sigma_f$ is the sweep speed of the source and it's given by the instantaneous phase $\theta(t)$ of the generated light as:

$$\sigma(t) = \frac{1}{2\pi}\frac{\partial\theta}{\partial t} \tag{2.18}$$

so

$$\theta(t) = 2\pi\int_0^t \sigma(t')\,dt' = \theta_0 + 2\pi f_0 t + \pi\sigma_f t^2. \tag{2.19}$$

Assuming that the emitted field is $E(t) = E_0 e^{i\theta(t)}$ and its power is constant,the measured intensity is

$$I_{meas}(t) \propto |E_0|^2 \left\{1 + |\rho_s(t)|^2 + 2Re\left[\int_0^L \rho(z)e^{[\theta(t-2z/c)-\theta(t)]}\,dz\right]\right\} \tag{2.20}$$

and considering that

$$\theta(t) - \theta(t-\tau) \approx 2\pi\sigma_f\tau t + 2\pi f_0\tau \tag{2.21}$$

the intensity measured by the detector is

$$I_{meas}(t) \approx |E_0|^2 \left\{1 + |\rho_s(t)|^2 + 2Re[b(t)]\right\} \tag{2.22}$$

where $\rho_s(t)$ represents the reflection coefficients of the sample and $b(t)$ is the beat term, which is proportional to the Fourier transform of the reflection profile:

$$b(t) = \int_{-\infty}^{\infty} \left[\rho(z)e^{-i4\pi f_0 z/c}\right] e^{-i4\pi\sigma_f t z/c}\,dz = F\left[\rho(z)e^{-i4\pi f_0 z/c}\right](2\sigma_f t/c). \tag{2.23}$$

Thus the reflection profile can be recovered by evaluating the inverse Fourier transform of the measured intensity $\rho(z) \propto |F^{-1}[I_{meas}(t)]|$.

From eq.2.23, the beat frequency is linearly dependant on the depth of the reflector, meanwhile when a real sample substitutes the reflector, multiple beat frequencies are detected, so the the reflectivity position can be reconstructed with a Fourier Transform.

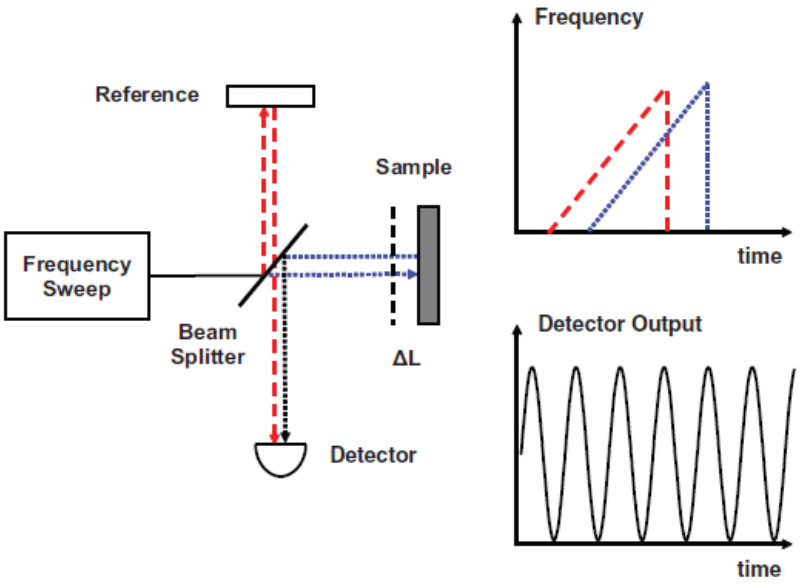


**Figure 2.10:** Diagram of a SS-OCT device.[3]

#### 2.3.2.1 K-CLOCK

Generally, a tunable laser is made up of a semiconductor optical amplifier (SOA), a tunable wavelength filter and a laser cavity. Through electrical signals, the tunable filter is set to the desired wavelength, making the frequency sweep. Quick changes in the selected wavelength can introduce non-linearity effects in the frequency sweep, due to mechanical motions, electric current modulation or a passive dispersive element, adding the nonlinear term $\eta(t)$ in Eq.2.17:

$$f(t) = f_0 + \sigma_f t + \eta(t). \tag{2.24}$$

In general, the non linearity induces a chirp in the signal at a constant depth, hindering the axial resolution.If the detector's output signal is digitized trough the DAQ device with a uniform clock signal, distortions in the images can appear, degrading the image quality. To overcome this issue, the detector's output can be sampled with a non uniform time interval though the so called *k-clock*. As shown in Fig.2.11, the k-clock signal is a timing control signal produced by an auxiliary Mach-Zehnder Interferometer (MZI), which detects the frequency-sweep and generates a frequency variable sinusoidal signal. Using the signal edges of the k-clock signal the sampling time of the OCT interferogram is automatically corrects, deleting the nonlinear sweep characteristics. Most of the current commercially available frequency-swept sources are

equipped with an internal MZI for the k-clock generation. Mathematically, part of the laser radiation is sent to the MZI, whose imbalance between the arms corresponds to a time delay $\tau_{MZI}$. The transmitted intensity can be written as:

$$I_{MZI}(t) \propto |E(t) + E(t - \tau_{MZI})|^2 = 2|E_0|^2 \{1 + \cos(2\pi\tau_{MZI} f(t)\} \tag{2.25}$$

Now let $t_1, t_2, ..., t_N$ be the time when the signal crosses the zero: when it happens, it means that the phase of the cosine has varied by $\pi$, so:

$$2\pi\tau_{MZI}\nu(t_{n+1}) - 2\pi\tau_{MZI}\nu(t_n) = \pi \tag{2.26}$$

and the frequency step

$$\delta\nu = \nu(t_{n+1}) - \nu(t_n) = \frac{1}{2\tau_{MZI}} \tag{2.27}$$

represents the times within the instantaneous frequency varied by fixed quantity. Thus, if the signal $I_{MZI}$ is samples at these times, it seems that the laser sweep is linear.

#### 2.3.2.2 Balanced detection

Substituting the diffraction gratings and the camera introduced in SD-OCT with simple photodetectors allows for a dual balanced detection scheme, improving the SNR ratio. As shown in Fig.2.11, once the signal collected by the the sample and the reference arm trough the circulators, they are sent to a 3dB fiber coupler, from which two interference signals can be obtained. Here, a balanced detector, can delete the common mode noise and at the same time summing the interference terms. This configuration can be associated to a Mach-Zehnder interferometer, which in these cases, is more efficient than a Michelson interferometer.

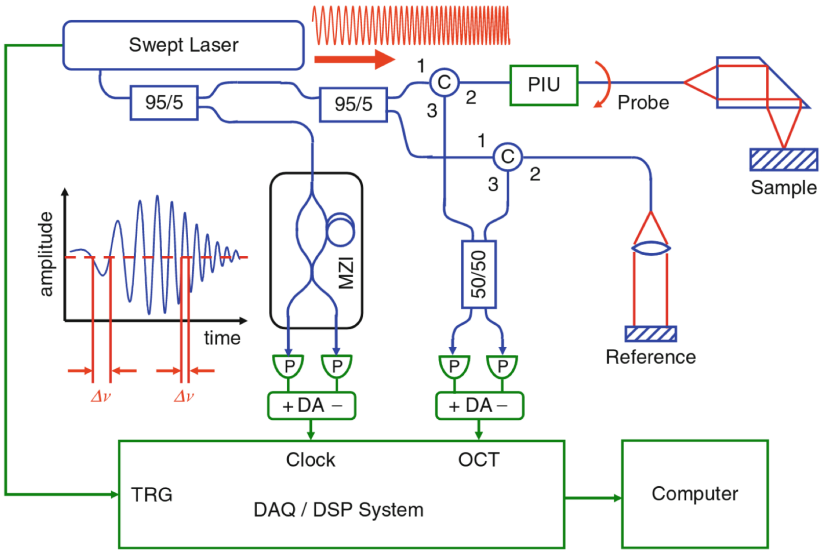


**Figure 2.11:** Balanced detection

## 2.4 Image characteristics

As an optical imaging technique, the quality of OCT is very strongly linked to the principles of optics. In this chapter, the most important features in the fields of optical imaging, microscopy and OCT will be illustrated.

### 2.4.1 Gaussian beam

Lasers commonly emit light beams with gaussian shape, that represents the lowest order and a radially symmetrical solution of the paraxial Helmontz equation. Related to the plane (x,y) perpendicular to the direction of propagation z, the field expression of a Gaussian beam can be written as

$$E_x(r,z) = E_0 \frac{z_R}{\sqrt{z^2+z_R^2}} e^{-\frac{kz_R r^2}{2\left(z^2+z_R^2\right)}} e^{i\left(kz+\frac{kzr^2}{2\left(z^2+z_R^2\right)}\tan^{-1}\frac{z}{z_R}\right)} \tag{2.28}$$

with the corresponding irradiance profile:

$$I_S(r) = I_0 e^{-\frac{2r^2}{w_0^2}} \tag{2.29}$$

where r is defined as the distance from the center of the beam and $z_R = \pi w_0^2/\lambda$ is the Rayleigh

range. Referring to equation 2.29 it can be extrapolated that the intensity is maximum for $z = r = 0$ and is equal to $E_0$, the beam increases in size slowly up to $z = z_R$ and then faster, while the radius of curvature is infinite at $z = 0$, has a minimum at $z = z_R$ and then increases proportionally to $z$. It can also be noted that all the considerations and equations deriving from eq.2.29 are also valid for negative values of z. with these premises, the propagation of a Gaussian beam can be schematized as in fig.2.12

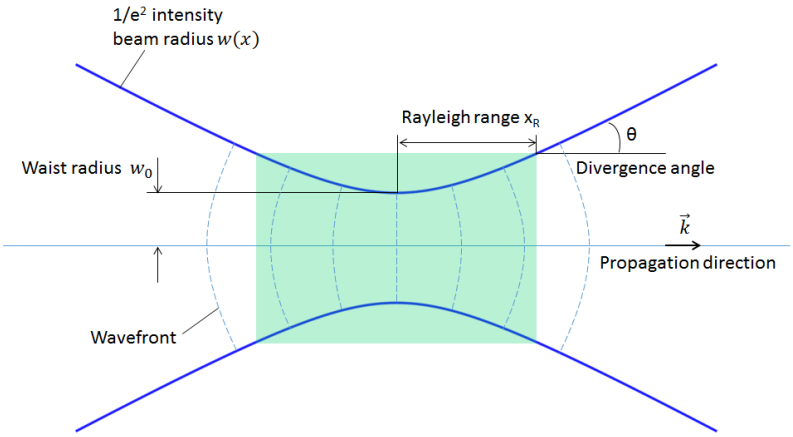


**Figure 2.12:** Propagation of a Gaussian beam

For this project, there are two important characteristics which come from eq.2.29: the focus spot size and the depth of focus (DOF). The first one is linked to the lateral resolution and it will explained in chap.2.4.2, meanwhile the second one refers to the range of distances along the optical axis of an optical system where objects appear sharp and well focused. Depth of field is affected by several factors such as f-number[1], wavelength , focal length, and numerical aperture(see eq.2.30, with NA=numerical aperture, f= lens focal length and D=lens diameter). In the treatment carried out up to now, the DOF coincides with the area delimited by the Rayleigh range, the point in which the beam radius becomes $w(z_R) = \sqrt{2}w_0$ and within which the beam is called collimated because the rays are all parallel.

$$DOF = 2z_R = \frac{2\lambda}{\pi}\left(\frac{1}{NA}\right)^2 = \frac{8\lambda}{\pi}\left(\frac{f}{D}\right)^2 \tag{2.30}$$

[1] defined as the ratio of focal length and the diameter of the entrance pupil[22]

### 2.4.2 Lateral resolution

As said in the previous section, Gaussian beam propagation is characterized also by a focus spot size, where the light is maximally concentrated and it can be defined by

$$2w_0 = \frac{4\lambda}{\pi}\frac{f}{D} = \frac{2\lambda}{\pi}\left(\frac{1}{NA}\right) \tag{2.31}$$

In the optical systems, the focus spot size identifies the lateral resolution. It describes how well an optical system can distinguish two nearby points or objects, along a direction parallel to the image plane. The higher the lateral resolution, the greater the system's ability to distinguish smaller and more subtle details, while a lower lateral resolution could result in blending or an inability to detect fine details. As it can be seen in eq.2.31, lateral resolution is determined by the numerical aperture NA and so by the lens focal length and its diameter, and by the wavelength $\lambda$. Therefore, lateral resolution can be improved by increasing the numerical aperture of the objective, but it can downgrade the DOF (see fig.2.13).

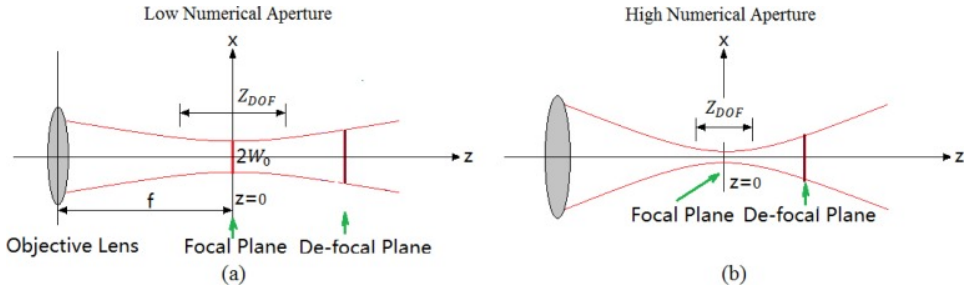


**Figure 2.13:** Effects of NA on lateral resolution[8]

Typically, OCT systems can achieve lateral resolution values smaller then $10\mu m$.

### 2.4.3 Depth resolution

One of the main advantages of OCT is represents by its axial resolution: unlike the traditional microscopy, it's not influenced by lens characteristic, but it's only determined by the light source. Indeed for a Gaussian PSD emitted by the source, axial resolution it's equal to its coherence length $l_c$, for the reasons explained in sec.2.2:

$$\delta z = l_c = \frac{2\ln 2}{\pi}\frac{\lambda^2}{\Delta\lambda} \tag{2.32}$$

where $\lambda$ is the center wavelength of source and $\Delta\lambda$ the spectral bandwidth. Hence, high values for axial resolution can be achieved regardless of the numerical aperture of the lens. Instead, to improve axial resolution, the spectral bandwidth must be increased and in parallel the wavelength must be decreased. However, there are some factors that degrade the axial resolution, for example, in materials with a high refractive index, as the wavelength becomes shorter, the actual axial resolution must be re-evaluated scaling the value by an appropriate coefficient. Other important factors to keep in mind on the decrease in the axial resolution are the same that cause dispersion of the signal:

- Group velocity dispersion (GVD): as it will described in Chap.4,it leads to various frequencies propagating with non-linearly related phase velocities and if a mismatch between the two arms exists, a brief pulse will become broader.

- Dispersion: in case of a single reflecting surface in sample arm in a FD-OCT device, the interference signal can be written as function of wavelenght as

$$I(\lambda) = I_r(\lambda) + I_s(\lambda) + 2\sqrt{I_r(\lambda)I_s(\lambda)}\cos\left(2f(\lambda)\Delta z + g(\lambda)\right) \tag{2.33}$$

  where $I_s$ and $I_r$ are the intensity of the sample and the reference arm light respectively, and $\Delta z$ is the the length difference between the two arms. The functions $f(\lambda)$ and $g(\lambda)$ are very important because the determine the resolution of the OCT system. In particular, assuming that a dispersion mismatch between two arms exists, and it's related to a material thickness $d$, $g(\lambda)$ can be written as $g(\lambda) = 2d/f(\lambda)(n(\lambda)-1)$ with the refractive index of the material equal to $n(\lambda)$ . To balance $g(\lambda)$ and achieve high axial resolution, $g(\lambda)$ must be balance, for example using the same material for both arms and if it is not sufficient, both hardware and software solutions exist. The function $f(\lambda)$ instead, represents the a nonlinear phase, which causes an degradation of the axial resolution due to the broadening of the coherence envelope in the time domain and it's mainly caused by misalignment, surface imperfections of the optics, dispersion of the diffraction grating and so on.

- Chromatic Aberration: conventional lenses have a focal length that is function of the wavelength and so the focal point is spread on different planes, altering the local effective bandwidth and so degrading the resolution.

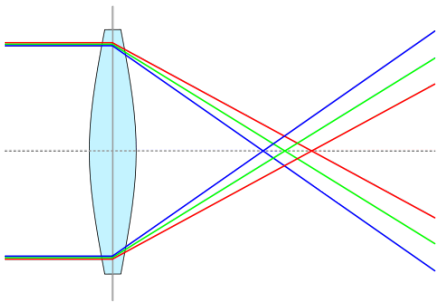

**Figure 2.14:** Chromatic aberration effects

Therefore it is useful to use suitably corrected achromatic lenses to maintain a wide spectral width, an unaltered optical band and a good axial resolution. In the ophthalmic OCT, chromatic aberration compensation must take into consideration the human eye as source of aberration.

- Polarization: the polarization mismatch between the arms of the OCT systems introduces a phase difference and therefore a different shape of the coherence function, getting a different axial resolution. Through polarization controllers(Sec.3.3.3) it's possible to compensate polarization changes, but it must be careful because the loss of a single polarization state and sample birefringence cause important modulations of the interference spectrum. [3]

## 2.5 Image acquisition

### 2.5.1 Scanning procedures

As in the ultrasound imaging techniques, also in OCT devices there are different ways to collect and visualize the data. As shown in Fig.2.15, the measurement of the tissue structures in depth at a single location is called A-line or A-scan. If the beam directed to the sample is scanned over a surface, several A-scan are taken, which together forms the two-dimensional cross-sectional OCT image, called B-scan. When several B-scans are collected side-by-side in a grid a complete three-dimensional data volume is obtained, in this case on can speaks about C-scan. As soon the C-scan is acquired, it's possible to visualize information about a single depth slicing crosswise the volume, with an so called en-face image. This type of images offers additional

advantages over conventional longitudinal cross-sections because it can delineate micro structural and morphological changes in coronal view, so precise measurements can be made, and it also provide a more extensive overview of pathological structures in a single image.

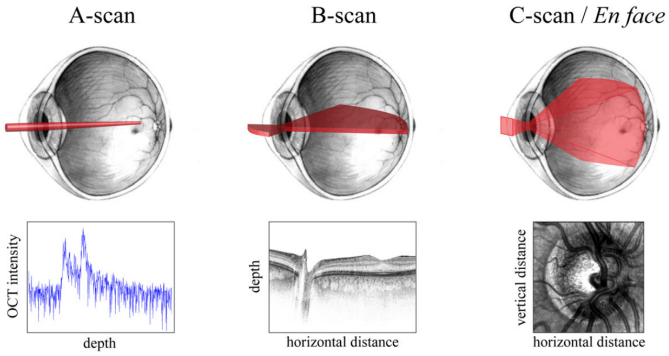


**Figure 2.15:** Example of A-scans(1D),B-scans(2D),C-scan(3D) and en-face image (on right bottom) of posterior eye[9]

### 2.5.2 Noise

The introduction of FD-OCT systems improved the imaging procedure both in terms of time and image quality. The improvement of SNR fits into this context, which will be briefly illustrated in this section. Generally the signal-to-noise ratio is defined as the signal power divided by the noise process variance. In order to simplify the analysis, the following considerations will be based on the use of a single reflection sample at position $z_S$, not considering the autocorrelation term without loss of generality. In these terms, when $L_R = z_S$, it can demonstrate that from Eq.2.14, the detected photocurrent of the mean square peak signal power of the effective OCT signals is:

$$\langle I_D \rangle^2_{TDOCT} = \frac{\mathcal{R}^2 S^2_{TDOCT}}{2} [R_s R_R] \tag{2.34}$$

where $\mathcal{R}$ is the detector responsivity, $S_{TDOCT}$ is the instantaneous source power incident in the sample arm and in the reference arm, $R_R$ and $R_S$ are the power reflectivity of the reflectors in the reference and in the sample arm. On the other side, in OCT systems noise comes from different sources. First of all there is the shot noise, described as electronic noise due to the corpuscular nature of the charges. Then there are the thermal noise and the flicker noise, and finally there the excess intensity noise coming from the laser source. As the shot noise is the fundamental limiting noise process for optical detection, the next considerations follow the ones used in shot noise limited design approaches. In an optical receiver the shot noise variance can be written as $\sigma^2_{sh} = 2e\bar{I}B$, where $e$ is the electronic charge, $\bar{I}$ is the mean detector

photocurrent and $B$ is the detection bandwidth. In an TD-OCT device, it can be written that $\sigma^2_{TDOCT} = \mathcal{R}eS_{TDOCT}R_R B_{TDOCT}$ where $B_{TDOCT}$ is the detection bandwidth of the TD-OCT device and it can be demonstrated that it must be half of the total autocorrelation term bandwidth. Thus, the SNR expression for a TD-OCT can be written as:

$$SNR_{TDOCT} = \frac{\langle I_D \rangle^2_{TDOCT}}{\sigma^2_{TDOCT}} = \frac{\mathcal{R}S_{TDOCT}R_S}{2eB_{TDOCT}} \tag{2.35}$$

This suggests that increasing the detection bandwidth, which means decreasing the scan duration or increasing the depth resolution or the scan range, worsen the SNR.

Similarly to the previous operations, it can be demonstrated that, from Eq.2.22 and extending the result to both SS-OCT and SD-OCT systems, the sampled version of the spectral interferogram is

$$I_D[k_m] = \frac{\mathcal{R}}{2} S_{FDOCT}[k_m] \left[ R_R + R_S + 2\sqrt{R_R R_S} \cos\left[2k_m(L_R - z_s)\right] \right] \tag{2.36}$$

where $S_{FDOCT}$ is the portion of the instantaneous power which arrives at the sample and it corresponds to the *mth* spectral channel of the detector, both in separate SD-OCT detectors and in SS-OCT time-multiplexed detectors.Evaluating the inverse Fourier transform of Eq.2.36 and considering only one single sampled reflector located at $z_S = L_R$, the mean-square peak signal power is

$$\langle i_D \rangle^2_{FDOCT} = \frac{\mathcal{R}^2 S^2_{FDOCT}[k_m]}{4} \left[R_R R_S\right] M^2 \tag{2.37}$$

where M is the number of pixels and obviously $m \in \{1, M\}$. As the same time, after the inverse discrete Fourier transform, the noise variance is given by $\sigma^2_{FDOCT} = e\mathcal{R}S_{FDOCT}[k_m]R_R B_{FDOCT}M$. Thus the SNR is

$$SNR_{FDOCT} = \frac{\langle i_D \rangle^2_{FDOCT}}{\sigma^2_{FDOCT}} = \frac{\mathcal{R}S_{FDOCT}[k_m]R_S}{4eB_{FDOCT}} M \tag{2.38}$$

Further considerations can be made to compare 2.38 in case of SS-OCT systems and SD-OCT systems to 2.35:

- In SS-OCT systems, since only one channel at a time is illuminated, for each of them the allowable sample illumination power is the same as the total illumination power in TD-OCT. So $S_{SSOCT}[k_m] = S_{TDOCT}$. Moreover the detection bandwidth in this case is limited by the D/A sampling frequency $\nu_s$. Also in this case, as in TD-OCT systems, the detection bandwidth must be limited to $\nu_s/2$ so $B_{SSOCT} = B_{TDOCT}$.

- In SD-OCT systems all spectral channels are illuminated simultaneously, so that the allowable power for each of them is inversely proportional to $M$, so $S_{SDOCT}[k_m] = {}^{STDOCT}/_{M}$ and it follows that $B_{SDOCT} = {}^{B_{TDOCT}}/_{M}$ as the signal from each channel are integrated over the entire A- line.

Thus, the SNR expression for FD-OCT systems are linked to the one of the TD-OCT system as

$$SNR_{SDOCT} = SNRSSOCT = SNR_{TDOCT}\frac{M}{2} \tag{2.39}$$

Considering that, devices available on the market have $M > 10^3$[3], it's clear how using FD-OCT has improved a lot the quality of the images.

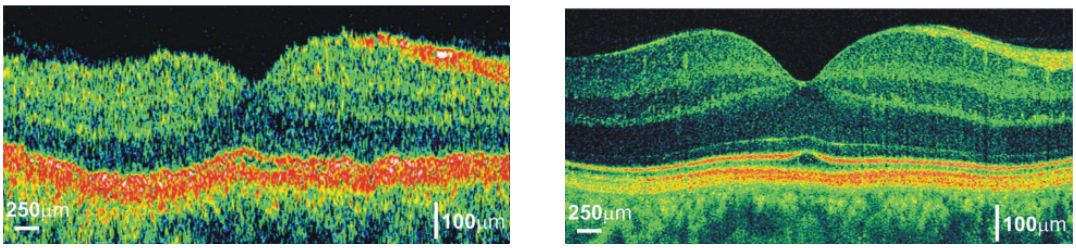


**(a)** time domain detection

**(b)** spectral domain detection

**Figure 2.16:** Comparison between TD-OCT and FD-OCT cross-sectional imaging of the human eye. The ginning visible in the first image is due to a lower SNR value. [1]

# 3 Setup

## 3.1 Setup overview

This chapter details the main parts of the Doppler Swept Source OCT implemented for the thesis work. As reported in fig.3.1, there's a part made up of optical devices, such as the laser source,couplers, circulator, and the optical fibers, and a part of acquisition and signal processing inherited from previous thesis works ([18]),briefly described in the last part of this chapter.

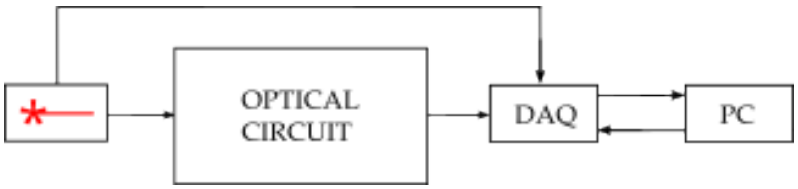


**Figure 3.1:** Diagram an SS-OCT system

## 3.2 Laser source

As already discussed in the previous chapter, the SS-OCT is based on a particular laser, which is capable to emit laser light with a continuously sweeping wavelength. In this project, the Axsun AXP50125-6 Swept Source Laser [10] was used, and it is showed in fig.3.2.


**Figure 3.2:** Axsun AXP50125-6[10]

### 3.2.1 Main characteristics

Axsun Technologies (now Excelitas Technologies[23]) provided several swept source engine laser, which differ from each other mainly in the central wavelength and the emitted power. The source laser chosen has the center wavelength equal to 1305nm and it's classified as a 3R class laser. Below are the main features of interest for the project:

**Table 3.1:** AXP50125-6 main parameters

| Parameter | value |
|---|---|
| Sweep Rate | 100 kHz |
| Center Wavelength | 1305.1 nm |
| Wavelength tuning range | 140.38 nm |
| Average power | 25.7 mW |
| Duty Cycle | 77.3% |
| Sampled Duty Cycle | 50.5% |
| External Clock Frequency | [183.1,332.1] MHz |
| Clock Max Frequency | 332.1 MHz |
| Sampling Clocks | 1536 |

From Tab.3.1 the expected edge wavelengths are $\lambda_1 \approx 1235nm$ and $\lambda_2 \approx 1375nm$. However, from the measures reported in [18][19], power remain constant in a smaller interval, so that the edges become $\lambda_1 = 1237$nm and $\lambda_2 = 1376$nm in reality. With these values, one can obtain

the the instantaneous frequency from

$$f(t) = f_0 + \sigma_f t \tag{3.1}$$

where $f_0$ is the starting frequency

$$f_0 = \frac{c_0}{\lambda_0 + \Delta\lambda//2} \approx 218.2THz \tag{3.2}$$

and $\sigma_f$ is the average sweep speed

$$\sigma_f = c_0 \left( \frac{1}{\lambda_0 - \Delta\lambda//2} - \frac{1}{\lambda_0 + \Delta\lambda//2} \right) \frac{f_a}{d_c} \approx 4.9THz/\mu s \tag{3.3}$$

with the sweep rate $f_a = 100$KHz and the duty cycle $d_c = 0.505$ taken from Tab.3.1.

### 3.2.2 Axial resolution

The choice of the laser swept source engine influences parameters such as DOF and lateral resolution, while it provides an estimate of the depth resolution, the value of which can be degraded if, for example, the chromatic dispersion should not be negligible. In particular, the first estimate of the depth resolution is given by:

$$\delta z \approx \frac{2\ln 2}{\pi} \frac{\lambda_0^2}{\Delta\lambda} = 5.37\mu m \tag{3.4}$$

### 3.2.3 Sweep trigger

One of the signals that AXP50125-6 can provides is the sweep trigger signal. It's a square wave used to sync the start of the frequency sweep and the acquisition of the A-scans. By connecting the appropriate output to the high-speed WaveSurfer 4024HD oscilloscope provided by Teledyne LeCroy[24], it was possible to acquire this signal and it's shown in Fig.3.3. In particular the voltage range measured $V_{trigger} \in [0, 1.42V]$ meanwhile the duty cycle is

$$d_{ctrigger} = \frac{t_H}{t_H + t_L} \approx 0.97 \tag{3.5}$$

since the signal stays at 0V for $t_L \approx 0.6\mu$s within a period of $t_H + t_L = 1//f_a = 20\mu$s.

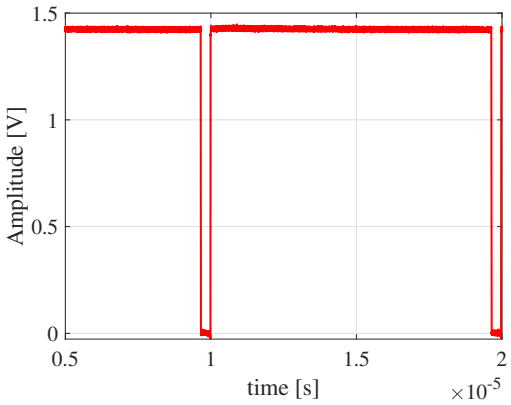


**Figure 3.3:** Sweep trigger signal of the Axsun AXP50125-6

### 3.2.4 Power profile

By using the photodetector described in sec.3.3.6, it's possible to measure the instantaneous power of the laser source and visualize it trough an oscilloscope. In particular, in Fig.3.4, the obtained power profile is reported with the trigger signal.

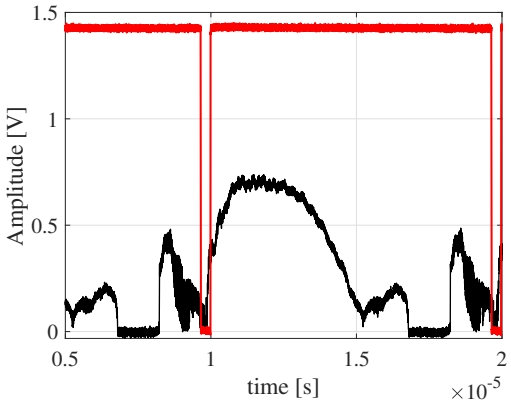


**Figure 3.4:** Power profile of the Axsun AXP50125-6

It can be seen that the power profile maintains the a regular profile for about 5$\mu$s, from which the value of the sampled duty cycle reported in Tab.3.1 comes from.

### 3.2.5 Clock

In the discussion in Sec.2.3.2.1, the importance of a k-clock signal in a SS-OCT device was explained. From Fig.3.5 it can be seen that the laser source used is equipped with an output channel capable of providing a variable frequency clock signal, thanks to its interzal MZI.

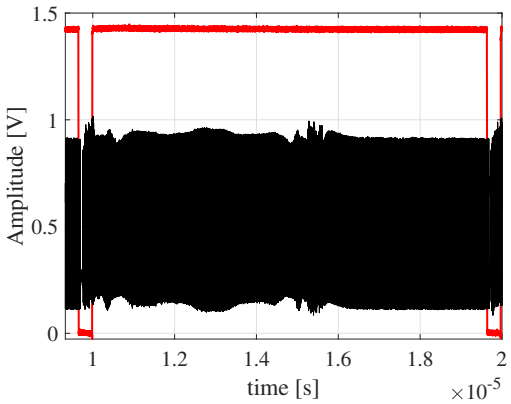


**Figure 3.5:** Clock signal of the Axsun AXP50125-6

The signal assumes value within the interval $[0.08, 1.02]$V with an average value equal to 0.50V. During the first 5$\mu$s, the sinusoidal clock drives the acquisition board in order to acquired 1536 samples as reported in Tab.3.1. In Fig.3.6, two different portions of the clock signal are shown, where the frequency varied. From3.6.a it's also possible to see that at the start of the acquisition, the clock signal is a bit distorted, but fortunately it doesn't compromise the performance.

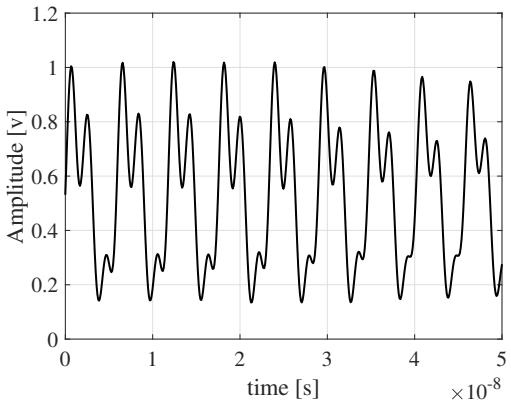


(a)

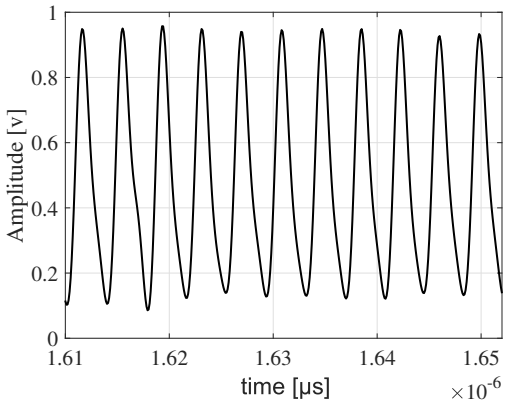


(b)

**Figure 3.6:** Behaviour of the k-clock signal at different time location

Moreover, from [19], the maximum clock frequency measured is 332MHz, from which is possible to evaluate the maximum imaging depth achievable by the system. Indeed the beat frequency generated by the signal overlap can be expressed by

$$f_{beat} = \sigma_f \tau \tag{3.6}$$

where $\sigma_f$ is the sweep speed introduced in Eq.3.3 and $\tau$ is the time delay between caused by the mismatch between the length of the reference arm and the sample arm. In particular $\tau$ can be expressed in term of the depth of a precisely layer that produces the echo trough the following way

$$\tau = \frac{2dn}{c_0} \tag{3.7}$$

where $n$ is the refractive index of the sample, $c_0$ is the light speed in vacuum and $d$ is the depth of the layer. Considering the Nyquist theorem, the maximum frequency that can be used to sampling the beat signal is half of the beat signal bandwidth, so that

$$f_{beat}^{max} = \frac{f_{clock}^{max}}{2} \tag{3.8}$$

which brings to the maximum depth (with $n = 1$):

$$d_{max} = \frac{c_0 f_{clock}^{max}}{4\sigma_f} \approx 5.1mm \tag{3.9}$$

This value satisfies the coherence length values reported in [19], whichis 12.3mm

## 3.3 Optical circuit

### 3.3.1 Optical fiber

The main component of an optical circuit is the optical fiber. In OCT systems, single-mode optical fiber is usually used and preferred because it allows the propagation of only one mode of light at a time and so OCT systems can achieve high spatial resolution, as the optical signal is focused on a single tissue point. Furthemore single mode optical fiber offers very low attenuation, which means that light can propagate through long distances with a minimum loss in power. Another critical point is dispersion: single-mode optical fiber has a low chromatic dispersion, which means that different colors of light travel with similar speeds along the fiber, maintaining spectrum integrity and keeping a good axial resolution. For the project, the choice fell on Corning®SMF-28e+®Optical Fiber[13], whose characteristics of interest for the research work are summarized in the following table:

**Table 3.2:** SMF-28e+®specifications[13]

| Specification | value |
|---|---|
| Max Attenutation (1310nm) | $\leq 0.35\ ^{dB}/_{Km}$ |
| Mode-Field Diameter (1310nm) | $9.2 \pm 0.4\,\mu m$ |
| Zero dispersion wavelength ($\lambda_0$ | $1304nm \leq \lambda_0 \leq 1324nm$ |
| Dispersion value (1559 nm) | $\leq 18^{ps}/_{(nm \cdot km)}$ |
| Zero dispersion slope($S_0$) | $\leq 0.092^{ps}/_{(nm^2 \cdot km)}$ |

### 3.3.2 Couplers

Once the signal has been sent by the laser source, it's necessary to divide it into two parts: one of them must go towards the sample, the other one must go to the reference arm. Simultaneously the signals deriving from the sample arm and from the reference arm must be recombined to be supplied to the balanced photodiode. The device which can perform these operations is a fiber optic coupler. In particular, it's a 4-ports passive device composed by two optical fibers fused together at a precise point.

For the first considerations an ideal behaviour has been considered including also the fact that ports 1 and 2 are isolated as are ports 3 and 4 as well, so that the scattering matrix is:

$$S = \begin{bmatrix} 0 & 0 & j\beta & \alpha \\ 0 & 0 & \alpha & j\beta \\ j\beta & \alpha & 0 & 0 \\ \alpha & j\beta & 0 & 0 \end{bmatrix} \tag{3.10}$$

The imaginary terms are due to the symmetric nature of the coupler chosen, so that straight paths such as $1 \longleftrightarrow 4$ and $2 \longleftrightarrow 3$ introduce just an optical power split without any phase shift, instead cross paths ($1 \longleftrightarrow 3$ and $2 \longleftrightarrow 4$) introduce a $\pi/2$ phase shift. Moreover, considering and ideal 50:50 split of optical power, the parameters become $\alpha = \beta = 1/\sqrt{2}$.In particular, the coupler chosen for the thesis is the TW1300R5A2 50:50 fiber coupler by Thorlabs which main specifications are reported in 3.3

**Table 3.3:** 50:50 Coupler specification[11]

| Specification | value |
|---|---|
| wavelength range | 1200-1400 nm |
| max insertion loss | 3.7 dB |
| coupling ratio | 50:50 |
| coupling ratio tolerance | ±5% |
| return loss | 60 dB MIN |

Before proceeding to introduce the coupler into the setup, some verification measures have been carried out. In particular, using a BPD(sec.3.3.6) and the ATS9350 digitizer(3.5.1) combined with the oscilloscope emulation software AlazarDSO provided by Alazar Technologies Inc.([25]), it has been possible to measure the power profile at the output of the laser source, then at port 2,3 and 4 using port 1 as input. As reported in Tab.3.4, the coupling ratio is not the ideal 50:50, but about 54% of the input power goes through the straight path to the port 4, instead the other 46% goes to port 3. It's important to underline that these values are in line with the ones given by the producer. For completeness, in Fig.3.7 the three power profiles measured are reported.

**Table 3.4:** Coupler measurements

| PORT1(IN) | PORT2(OUT) | PORT3(OUT) | PORT4(OUT) |
|---|---|---|---|
| 12.6dBm | -44dBm | 9.3dBm | 9.9dBm |

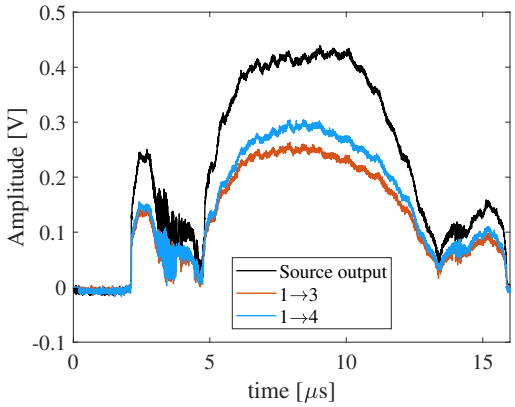


**Figure 3.7:** Power profiles trough the coupler

In the optical circuit the TW1300R5A2 50:50 fiber coupler is placed just before the BPD, meanwhile after the laser source the TW1300R2A2 90:10 fiber coupler is used. This particular choiche is due to the need of optimizing the use of the signal. Indeed, splitting the signal midway would have used more than necessary for the reference arm, while decreasing the SNR in the sample arm. Whereas with a 90/10 split of the signal, the majority of the signal is sent to the sample arm, while the remaining small part is used by the reference arm.

### 3.3.3 Polarization control

As explained in Cap.2, polarization control is needed to maintain control over polarization mismatch between the two arms of the interferometer, in order to achieve a good quality image. For this project it was decided to use the MPC320 - Motorized Fiber Polarization Controller by Thorlabs (Fig.3.8).

**Figure 3.8:** MPC320 by Thorlabs[11]

This particular type of polarization controller exploits the bending-induced birefringence to alter the polarization in the fiber thanks to three independent fractional wave plates created by winding three independent spools with a precise number of loops. In this way, the fast axis of the fiber lays in the plane of the spool and it can be adjusted with respect to the polarization vector by simply rotating the spools to twist the fiber. Fiber cladding diameter, the spool diameter, the number of fiber loops per spool and the wavelength are the factors that control the amount of the birefringence induced in the fiber. In particular, to transform a random polarization state into a defined output polarization state, the controller uses a combinations of three paddles: a quarter-wave plate, an half wave plate and another quarter-wave plate in series. The first quarter-wave plate transforms the input polarization state into a linear polarization

state, the half wave plate rotates the linear polarization and the final plate would transform the linear state into a desired polarization state. To derive the right number of loops for each spool the following equation must be taken into consideration

$$\varphi(radians) = \frac{2\pi^2 aNd^2}{\lambda D} \tag{3.11}$$

which estimates the retardance $\varphi$ of each paddle, with is a constant (equal to 0.133 for silica fiber), N is the number of the loops, d is the fiber cladding diameter, D is the loop diamater and $\lambda$ is the wavelength. So, considering the SMF28e+ fiber previously described, in order to obtain the desired sequence of wave plates, it was necessary to do two wraps for $1/4\lambda$ retardation and 3 loops for $1/2\lambda$ retardation. Thorlabs provides also the Kinesis software suite, whose user interface allows full control of all operating modes and settings, so as to allow complete "out-of-box" operation. In fact it provides all the necessary system software services such as generating GUI panels, managing communications for multiple USB drives and monitoring all system activities in order to help in hardware troubleshooting (Fig.3.9).

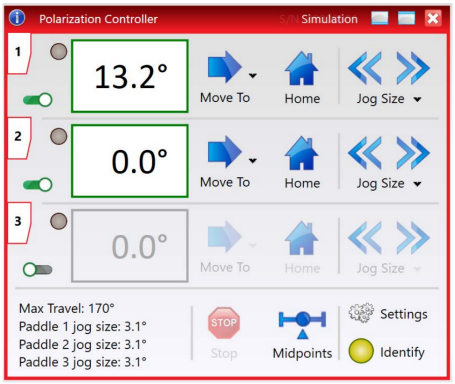


**Figure 3.9:** MPC320 GUI Panel

### 3.3.4 Circulator

In order to isolate the laser source from possible unwanted reflections coming from the sample arm (Fig.3.31), it has been necessary to insert an optical circulator just after the optical divider. It's a three-port device that allows light to travel in only one direction at a time, in fact the general scattering matrix for a lossless, matched circulator is:

$$S = \begin{bmatrix} 0 & 0 & 1 \\ 1 & 0 & 0 \\ 0 & 1 & 0 \end{bmatrix} \tag{3.12}$$

For the thesis, a lossy three port network with isolation between output ports(2 and 3) has been chosen, so S13 term becomes equal to 0. In particular, the choice fell on CIR-1310-50-APC fiber optic circulator made by Thorlabs [11]. It's a non-reciprocating, one directional, three- port device which provides, as reported in Tab.3.5, low insertion loss, high isolation, high return loss.

**Table 3.5:** Circulator specification[11]

| Specification | value |
|---|---|
| wavelength range | 1280-1400 nm |
| max insertion loss($1 \rightarrow 2, 2 \rightarrow 3$) | 1.6 |
| isolation($2 \rightarrow 1,3 \rightarrow 2$) | 28 dB MIN |
| directivity ($1 \rightarrow 3$) | 50 dB MIN |
| return loss | 45 dB MIN |

To prove the specifications, before inserting the device into the setup, verification measurements were carried out and the results are reported in 3.6. The reference valued obtained connecting laser source directly to the power meter was 12.8 dBm and all the inputs were connected in turn to analyze the power outputs. So that it could be concluded that the specifications are met.

**Table 3.6:** Circulator measurements

| - | INPUT1 | INPUT2 | INPUT3 |
|---|---|---|---|
| OUTPUT 1 | - | -30dBm | -53dBm |
| OUTPUT2 | 12.4dBm | - | -30.3dBm |
| OUTPUT3 | -44dBm | 12.7dBm | - |

It's interesting also to notice the power profiles reported in 3.10. In this case the laser source was connected to port1 at first and then to the port2, and the outputs were connected,to

ATS9350 digitizer through the DET08CFC/M photodetector by Thorlabs and the curves were displayed with AlazarDSO software.

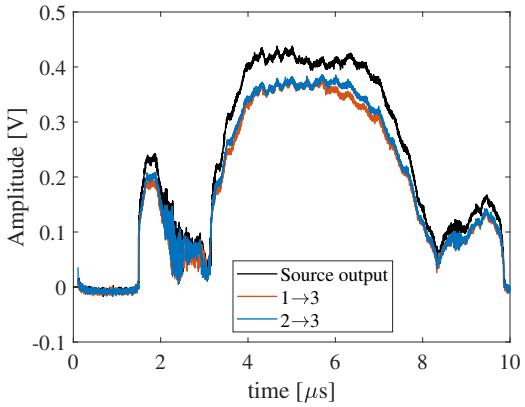


**Figure 3.10:** Power profiles trough the circulator

### 3.3.5 Variable Optical Attenuator

In a Mach-Zehnder interferometer, the balance between the two arms is fundamental to achieve useful interference results. If one of the arms has much more power than the other one, the interferometer behaviour can be negatively influenced. For example, an high power value coming from one of the two arms can saturate the detector, making impossible to detect intensity variations caused by reflection or scattering of light in the sample arm. Moreover a sample arm with low power means the signal reflected by the sample would be much weaker compared to the reference arm's signal and this significantly reduces the sensitivity of the interferometer in detecting phase variations in the signal reflected from the sample, degrading the ability to detect structural detail or change in reflectivity. So, obtain reliable results it is crucial to balance the power mismatch between the reference arm and the sample arm. In this work it was introduced in the reference arm the Thorlabs' fiber-coupled electronic variable optical attenuators (VOA) 1550A, designed to enable simple voltage control of optical power. Attenuation is controlled by means of the voltage supplied to the device via a BNC cable connected to the NI 6211 introduced in sec.3.5.3 with a DC or a AC modulated voltage up to 1 kHz whose amplitude must stay between 0 and 5 V. All the other specifications are reported in Tab.3.7.

**Table 3.7:** V1550A by Thorlabs specifications[11]

| Specification | value |
|---|---|
| Wavelength Range | $1250 - 1650$ nm |
| Max Attenutation | $> 25$ dB |
| Min Attenuation | 1.5 dB |
| Optical Input Power (Max) | 100 mW |
| Optical Return Loss | $> 30$ dB |

### 3.3.6 Photodetector

The method of balanced detection, as discussed in sec.2.3.2.2, has been developed for small differences between two optical input signals. For this work, the BPD-1 photodetector by Insight (Fig.3.11.a) was chosen [26]. It's a differential photodetector, whose band goes from 0 to 400 MHz and it's optimized for SS-OCT imaging systems. As shown in the simplify scheme 3.11.b,it's made up of two balanced photodiodes connected in series in order to achieve an high common mode rejection ratio (CMRR) and an ultra-low-noise, high-speed transimpedance amplifier which amplifies the signal difference between the two diodes and given as output through the RF-output port. It's also equipped with a Monitor+ and a Monitor- port which allow to observe the response of each photodiode independently.

#### 3.3.6.1 Responsivity

Once the power signal coming from the optical fiber arrives to the input port, through the photodiode, it is translated into current through a conversion quantity called responsivity. In particular is defined as the ratio between the generated photocurrent and the incident optical power:

$$\mathcal{R} = \eta \frac{e}{hf} \tag{3.13}$$

where $hf$ is the photon energy, $\eta$ is the quantum efficiency and $e$ the elementary charge, so the unit of measurement is $A/W$. Normally the producers provide the responsivity curve with their photodetectors. In this case Insight declares a responsivity equal to $0.85 mA/mW$ at $1310 nm$ coupled with an FC/APC fiber optic.

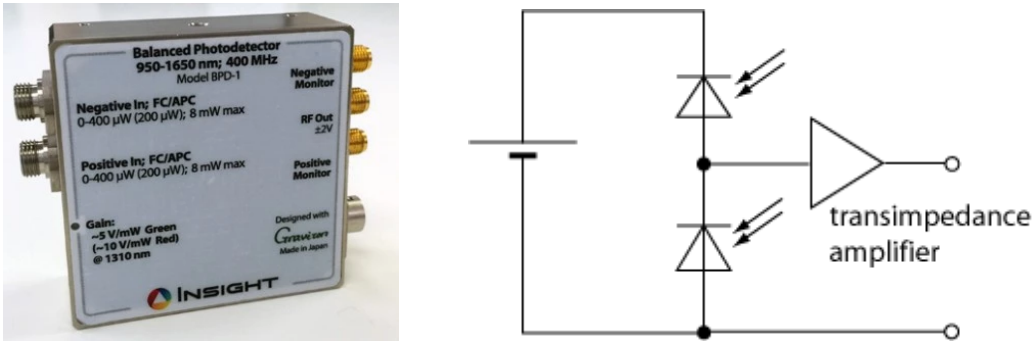


**(a)** BPD-1 by Insight[26]

**(b)** Simplified scheme of a photodetector

**Figure 3.11:** Photodetector used(a) and its simplified scheme(b)

### 3.3.6.2 Thermal noise

In the treatment of sec.2.5.2, all noise sources apart the ones of the shot noise were neglected. However, reality differs slightly from the case presented, but the equations remain valid. What can lead to a worsening of the SNR value can be the thermal noise of the acquisition card, or in this case of the photodetector. Obtaining this quantity can be fundamental in the case of very small powers. In this work, to carry out the measurement of this work, the photodetector was connected to the acquisition card presented in sec.3.5 and, keeping the photodetector off, a measurement of 16ms was carried out. Once carried out, the measurement was repeated by powering the photodetector. in Fig.3.12 we can see the power spectral density measured in both cases: in particular we can see that once the photodetector is turned on, the PSD goes from an average value of $-131$dB//Hz to the value $-125$dB//Hz, which is pretty low.

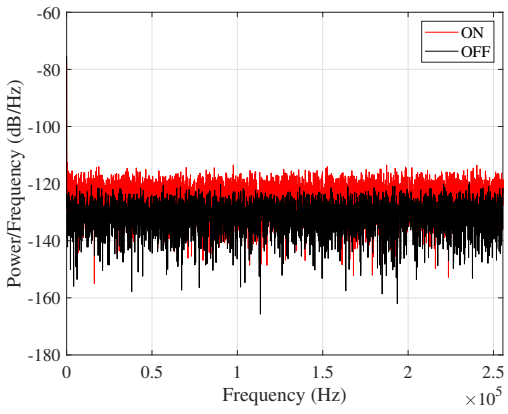


**Figure 3.12:** Power spectral density of BPD-1 by Insight

## 3.4 Scanning system

Once the laser pulses travel through the sample arm, they arrive at the scanning head, which has the task of scanning the entire biological sample.It is mainly composed of 3 main elements:

- a collimator, which ensures that ensures that the beam rays are parallel when they get the mirrors of the next element;
- galvo system, made up of two servo motors on which two mirrors are mounted in order to to direct the beam;
- focusing lens, which focus the beam on the sample.

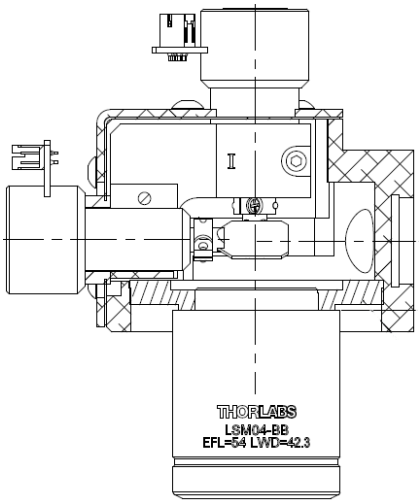


**Figure 3.13:** Scanning system[11]

### 3.4.1 Collimator

The collimator has the task of collecting the light coming from the fiber and collimate the beam on the galvanometric mirrors. In real there's a small divergence angle given by the following equation whenever the beam has a Gaussian intensity profile:

$$\theta \approx \frac{D}{f}\frac{180}{\pi}[^\circ] \tag{3.14}$$

where D is the mode-field diameter and f is the focal length of the collimator.It works well only with single mode fiber, but it gives an underestimate value for multimode fiber with

non-Gaussian beam profile. For the development of this project, the collimator used is the F280APC-C by Thorlabs[11] (Fig.3.14), designed for center wavelength of 1310 nm. The other specifications are reported in Tab.3.8:

**Figure 3.14:** F280APC-C[11]

| PARAMETER | VALUE |
|---|---|
| Central wavelength | 1310 nm |
| Waist diameter | 3.4 mm |
| Numerical aperture (NA) | 0.15 |
| Focal length | 18.67mm |
| Divergence angle | 0.028° |

**Table 3.8:** F280APC-C specifications

### 3.4.2 Galvo system

The collimated beam arrives at the galvo system made up of a galvanometer-based motor with a scanning mirrors mounted on the shaft and a detector that provides positional feedback to the control board. A galvanometer is a precision motor with a travel of few degrees, whose acceleration and shift are proportional to the current provided from its control board. The mirrors are mounted at the end of the actuator and deflects the light within the angular range of the actuator shaft. Since the applications of this particular system demand high speed and high frequencies of the shaft rotation, the inertia of the system actuactor+mirror can have a major impact on system performance. In order not to have to deal with these problems, the choice fell on Thorlabs GVS002 scanning galvo system, where the previous described problems have been precisely balanced. In Fig.3.15 is reported the system made up of two actuators and two mirrors, one for each scanning axis.

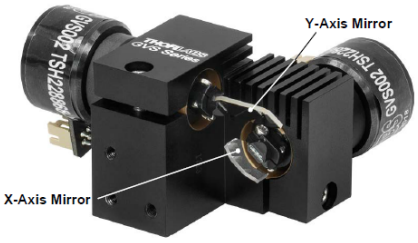


**Figure 3.15:** GVS002 dual axis galvo system[11]

Thorlabs also provided the control boards useful to control the servomotors and make useful diagnosis in case of suspected fault. In particular the servo circuit read the position signal coming from optical sensors position and use the error signal, speed and integral of current terms to output control voltages so it can drive the actuator to ideal position. In Fig.3.16 is reported the control board used to control one of the servos and the useful connectors.

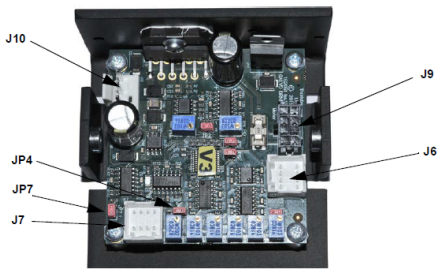


**Figure 3.16:** GVS002 control board[11]

In the figure also a portion of the heat sink can be seen, essential to keep the temperature below $50°C$, above which the possibility of faults of actuators functioning increases. A very detailed description of electronic circuits is found in [18] .

### 3.4.3 Analysis of the position error

Before introducing the entire scanning system in the acquisition circuit, it ha been necessary to analyze the position error of the mirror, because eventually it must be compensated by the software which control the entire device. In particular, the aim of the analysis is to see if the error position is somehow constant, or if it changes proportional to the servo speed, position, the frequency and amplitude of the command signal. For this purpose, the analysis setup is made up of National Instruments NI6343 I/O multifunction device (described in Sec.3.5), the galvo system with his controls board and a PC with Matlab software. The latter is used to control

the NI6343, which is responsible to generate control signal and collect the diagnosis ones from the control boards. The main control boards connectors used for this aim are the J7-command signal connector and J6-diagnosis connector (see Fig.3.16), according to the following scheme:

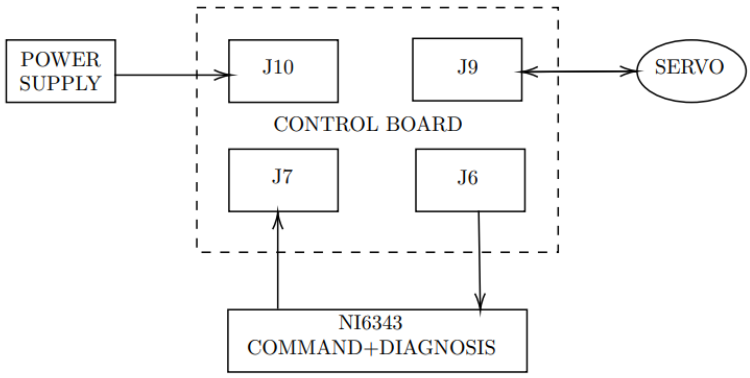


**Figure 3.17:** Control board connection

The command signal required must have some particular characteristics, which will now be explained. The recommended mechanical scanning angles for a beam diameter equal to 3.4mm are in the interval $[\pm 9°]$ for x axis and $[\pm 12.5°]$ for y axis. In addition, control board required at maximum an absolute value of 10V, which corresponds, once the jumper of JP7 connector (see Fig.3.16) has been set to $1V/°$ scaling factor, to the mechanical scan range $[-10°, +10°]$. As it will explained in Sec.3.4.4, the maximum optical scan angle supported by the focusing lens is $\pm 7.5° \times \pm 7.5°$, so it represents the main limitation for the scan area and so for the amplitude of the command signal. In particular, considering that the scan angle is twice the mechanical one, the voltage required for the actuators must stay within the interval $[\pm 3.75V]$ and this is the first characteristic of the command signal. Then, considering that the laser has a 100kHz sweep rate, it is necessary to implement a sawtooth signal instead a triangular one, so that the duration of the mirror return phase is minimized. The purpose of this analysis is to investigate the behaviour of the error signal coming from J6 connector (3.16). In particular, the first thing to see is the range within which the frequency must lie, then to see if the position error increases just in some particular positions or it is constant, in order to well compensate it through the final acquisition software. To simulate the final implementation, one of the mirrors is controlled to make B-scans (controlled by the sawtooth signal), instead the other one must move the B-scan line in the closest parallel one (controlled with a modified staircase signal).

In order to see if there are some particular differences between the two actuactors, each exam has been executed using both the axis as B-scan axis in turns. So signals in Fig.3.18 are the ones implemented in differential mode to command the galvo system, acting on their frequency:

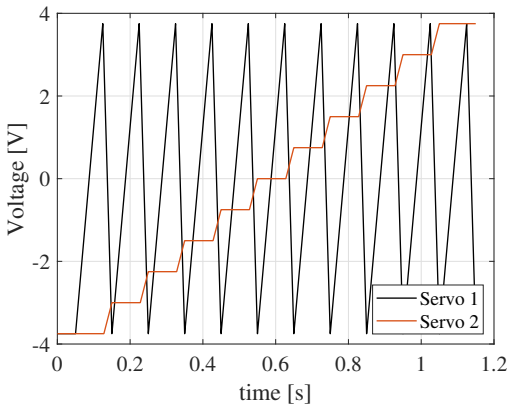


**Figure 3.18:** B-scan command signal

Each test has been repeated from 10 to 60 frame/s with an increment of 10. In Fig.3.19 and in Fig.3.20 are reported the error signals for both the galvo motors at 30 frame/s and in particular, the motor wich controls the direction of the laser beam along the x-axis was piloted with the sawtooth signal, meanwhile the staircase one controlled the motor responsible for the y-axis orientation. In both of the cases also a zoom version of the result is reported and comparable results was found by inverting the command signals. In each direction, two main aspects come out from the error signals: the first one is that there's a drift of the signals which seems to stabilize after 20 seconds and the second one is that every movement causes position error, infact in Fig 3.19.b there are different values depending if the mirror is moving in one direction or the other, and this is repeated in Fig.3.20.b with smaller values.

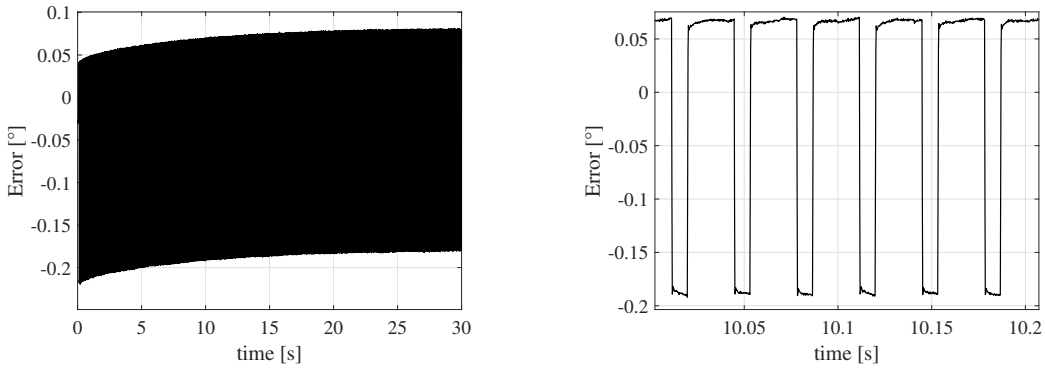


**(a)** X-axis error

**(b)** X-axis error (zoom)

**Figure 3.19:** X-axis error and zoomed version

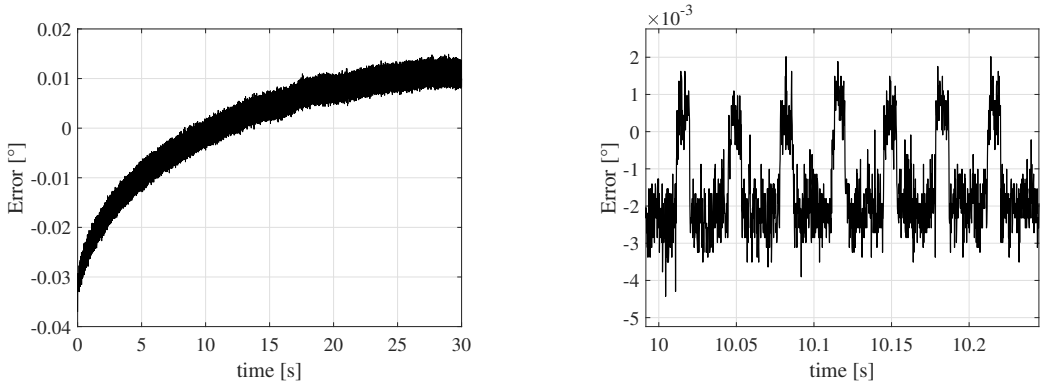


**(a)** Y-axis error

**(b)** Y-axis error (zoom)

**Figure 3.20:** Y-axis error and zoomed version

#### 3.4.3.1 Mechanical angle vs scan error

From Fig.3.19 and Fig.3.20 it's clear that the error in the mirrors position suffers the direction of movement since they have a behaviour similar to a square wave, and a time cumulative factor which increasingly deviates the real position from the estimated one as time passes. Indeed, at the beginning of the acquisition, the error of the X-axis stay within the range $[-0.21°, +0.04°]$ meanwhile after 30s the interval edges have settled to $[-0.18°, +0.75°]$. At the same time, Y-axis error goes from $[-0.03°, -0.02°]$ to $[+0.009°, +0.01°]$ error interval. In order to relate the mechanical angle applied to the mirror and the beam spot position on the focal plane, it

can be used the following equations:

$$x = EFL \tan\left(2\theta_{m,x}\right) \tag{3.15}$$

$$y = EFL \tan\left(2\theta_{m,y}\right) \tag{3.16}$$

which determined the position along the $x$ and the $y$ position. In particular EFL is the effective focal length defined in the next section and and $\theta_m$ is the mechanical angle of the mirror responsible for scanning along one of the two directions. At the same time, Eq.3.15 and Eq.3.16 are useful to determine the error in the position on the focal plane, so considering the maximum absolute value for the mechanical angle for each direction, the maximum position errors on the focal plane are:

$$\delta x_{max} = EFL \tan\left(2 \cdot 0.75°\right) = 1.414mm \tag{3.17}$$

$$\delta y_{max} = EFL \tan\left(2 \cdot 0.03°\right) = 0.057mm \tag{3.18}$$

The value $\delta x_{max}$ seems to be large but it must considered that acquisitions take much less time to be performed. Indeed, considering a scan time of 10 seconds, and keeping the X-axis the one within the B-scans are performed and the Y-axis the direction in which the shift occurs between each B-scan, the resulting errors for the extreme conditions of 10 frame/s and 60 frame/s are:

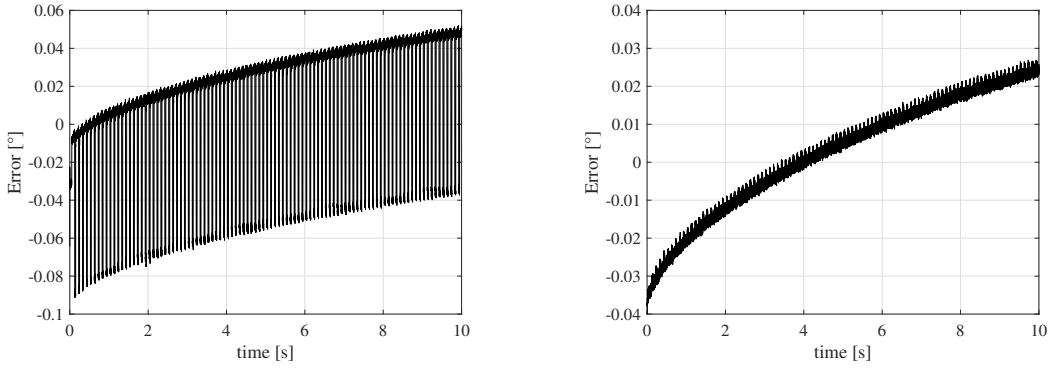


**(a)** X-axis error

**(b)** Y-axis error

**Figure 3.21:** Error signals at 10 frame/s

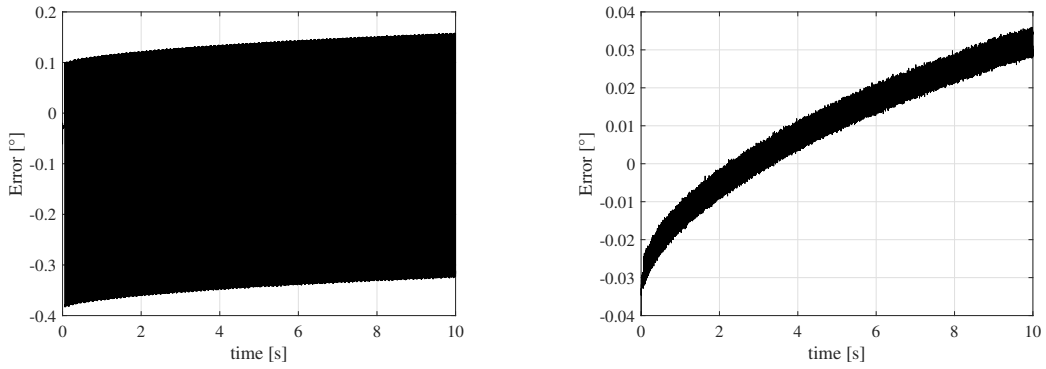


**(a)** X-axis error **(b)** Y-axis error

**Figure 3.22:** Error signals at 60 frame/s

From which it can be seen that $\max\{|\theta_{m,x}|\}$ goes from $0.09°$ at 10 frame/s to $0.38°$ at 60 frame/s and $\max\{|\theta_{m,y}|\}$ is equal for both acquisitions and it's equal to $0.03°$. This means that $\delta x_{max}$ increases as the frame rate increases and in particular $\delta x_{max} \in [0.16, 0.71]$mm, meanwhile $\delta y_{max}$ remains constant at $0.057$mm.

Wanting to investigate any construction differences between the two servomotors that could justify such error differences, the driving signals were inverted in order to have B-scans carried out along the Y-axis with lateral movement along the X-axis. Also in this case the extreme cases at 10 frame/s and 30 frame/s are reported:

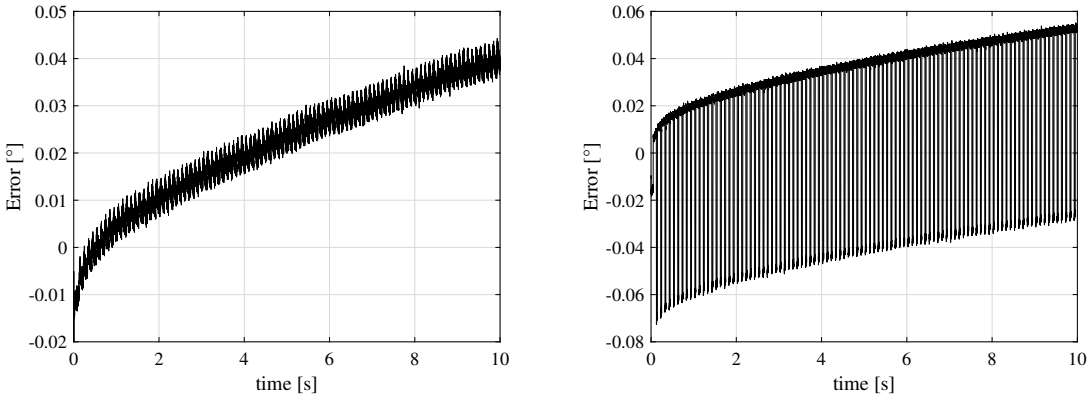


**(a)** X-axis error **(b)** Y-axis error

**Figure 3.23:** Error signals at 10 frame/s

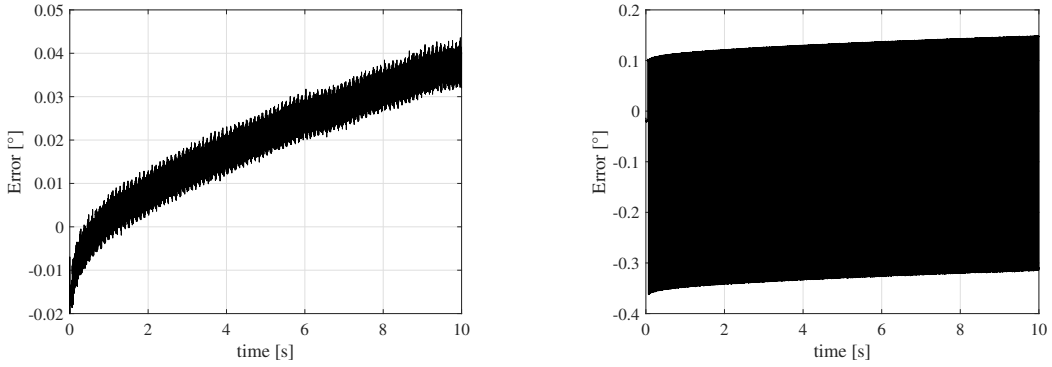


**(a)** X-axis error

**(b)** Y-axis error

**Figure 3.24:** Error signals at 60 frame/s

In this case $\delta x_{max}$ remains constant at 0.075mm meanwhile $\delta y_{max} \in [0.13, 0.68]$mm. Thus, feeding the two servos with the same signal brings to have comparable error values, which means that the two servo are totally equal, meanwhile the difference between the two errors is due to the pilot signal.

### 3.4.4 Focusing lens

The last component of the scanning head is the scan lens and in particular, a tele-centric lens was used. Unlike conventional lenses, telecentric scanning lenses block the parallelism of light rays passing through the lens, minimizing the effect of perspective and optical distortions. This property is particular useful in in areas such as OCT, where the viewing angle should not affect the apparent size of the object. Infact, they can reduce the distortions that occur with traditional lenses when objects are off the optical axis. The main parameters that characterize this particular device are:

- Entrance Pupil Size (EP): also known as back aperture, its size specifies the diameter of the collimated laser beam that maximes the resolution of the imaging device.
- Scan Angle (SA): it indicates the incident beam angle coming from the mirrors respect to the optical axis of the lens.
- Scanning Distance (SD): it is the distance between the EP plane and the base of the lens.
- Depth of View (DOV): it is the distance between the the the parallel planes where the beam spot diameter is $\sqrt{2}$ greater than it is ath the focal plane.

- Field of View (FOV): it represents the maximum size of the area on the sample that can be imaged with a resolution equal to or better than the stated resolution of the scan lenses.

- Parfocal Distance (PD): it is the distance from the scan lens mounting plane to the front focal plane of the scan lens.

- Working Distance (WD): the distance between the tip of the scanning lens housing and the front focal plane of the scanning lens.

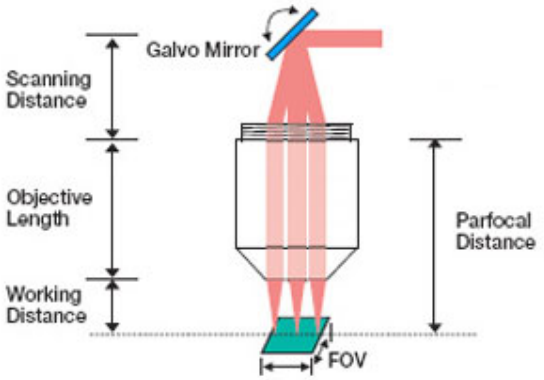


**Figure 3.25:** Telecentric lens diagram [11]

For the SS-OCT system developed in this project, the Thorlabs LSM04 lens was used. All the main specification are reported in Tab.3.9. It's interesting to noting the FOV value, which is the main cause of the limitation of the driving voltage of servo motors. In fact, as explained in sec.3.4.3, using the previously declared values and equations 3.15 and 3.16, the obtained FOV is exactly equal to the one reported in the datasheet.

**Table 3.9:** LSM04 by Thorlabs specifications[11]

| Specification | value |
|---|---|
| Wavelength range | $1250 - 1380$ nm |
| Effective Focal Length (EFL) | 54 mm |
| EP | 4 mm |
| Maximum Scan Angle | $\pm 7.5° \times \pm 7.5°$ |
| FOV | $14.1 \times 14.12$ mm$^2$ |
| DOV | 0.61 mm |
| PD | 80.8 mm |
| WD | 42.3 mm |

## 3.5 Data Acquisition and Signal processing

The entire part of data acquisition and signal processing is based mainly on two devices, the NI6343 I/O multifunction device provided by National Instruments([14], and the 12-bit ATS 9350 waveform digitizer board made by AlazarTech([12]). In particular the GUI, as the part of the C++ acquisition software developed in [19], initiates an acquisition by communicating with the ATS9350 board and the NI6343, which is dedicated to control the galvo mirrors and to supply the "frame start" signal. Once this signal arrives to the AT9350, this one listens for A-scan triggers provided by the laser source and start sampling the interference signal through the k-clock. Once the an entire B-scan is acquired, the board return the data to the application, which process, display and save them to disk. To these two main devices, another I/O multi-function device was added to the system in order to control the VOA: it is the NI6211 made by National Instruments.

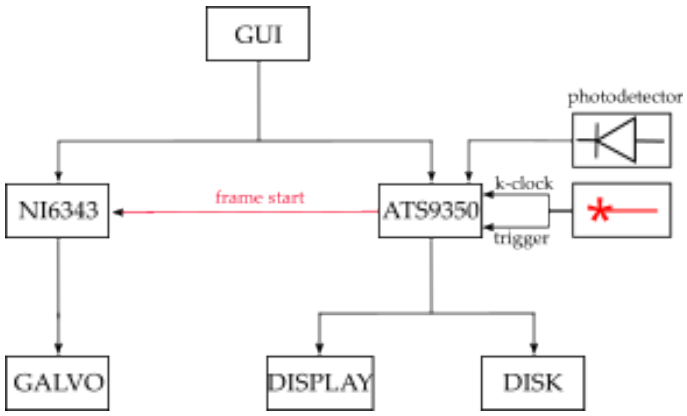


**Figure 3.26:** Diagram explanation of how the system is implemented

### 3.5.1 ATS9350

**Figure 3.27:** ATS9350 by AlazaTech[12]

As said previously, in order to digitize the interference signals coming from the OCT device, an high speed and specialized DAQ device is required. The one used for this thesis is the AlazarTEch ATS9350, which is designed, among other things, for OCT applications. It has the following characteristics:

- 8-lane PCI Express 2.0 (PCIe x8) card
- 250 MHz input bandwidth

- 12 bits sample resolution
- external trigger support
- Variable frequency external clocking
- 500 MS/s real-time sampling rate
- $\pm$40mV to $\pm$4V input range with an input impedance of 50$\Omega$
- 2 input channel with a dedicated ADC chip and a user-selectable sampling rate from 2MHz up to 500MHz. Full acquisition speed 2ch$\times$500MS/s$\times$2 bytes per sample=2 GB/s.
- On board FPGA module for the computation of the FFT

The board is given with the proprietary AlazarDSO software to configure the device, then to acquire and display signals.The device was installed in a Dell Precision T5810 workstation with:

- 16GB DDR4 ECC RAM at 2400MHz
- 256GB DATA SSD
- Intel Xeon E5-1650 V4, 3.6GHz, 6 cores and 12 threads
- NVIDIA Quadro M4000 with 8GB of DDR5 memory

### 3.5.2 NI6343

**Figure 3.28:** NI6343 by Nation Instruments[**?** ]

In order to control the optical head servo motors, a device which acts as and intermediary between the PC and the galvo control board is needed. For this purpose, the choice of a I/O multifunction device such as the NI6343 was the best one thank to its characteristics which will be discussed in this section. In particular the each galvo board needs 5 free pins: two analog output pins used to provide differential signals like the ones in Fig.3.18, one digital output pin used to provide the external enable signal (+5V) useful to activated the external control on the servo and finally two analog input pins for ground. All the data are transferred from and to the PC through an USB port. The main characteristics of the two types of analog channel are reported below:

**Table 3.10:** Analog Input channels characteristics[14]

| Specification | value |
|---|---|
| Number of channels | 32 single ended or 16 differential |
| ADC resolution | 16 bits |
| Sample rate | 500 kSample/s |
| timing resolution | 10 ns |
| Maximum working voltage | ±11 V of AI GND |

**Table 3.11:** Analog Output channels characteristics[14]

| Specification | value |
|---|---|
| Number of channels | 4 |
| DAC resolution | 16 bits |
| Maximum update rate (4 channels) | 719 kSample/s |
| timing resolution | 10 ns |
| Output range | ±10 V |

#### 3.5.2.1 Read and write procedures

The control of the device via C++ was the subject of the previous theses already mentioned. During this work, in order to analyze the error of the servomotors, a matlab script was developed capable of controlling the reading and writing processes of the NI6343 via the "Data Acquisition Toolbox Support Package for National Instruments® NI-DAQmx Devices"[27]

toolbox and therefore the data transmitted and collected from the servomotor boards. All this to streamline and accelerate the analysis process without going through C++ software.

Once the device is connected, the first command to execute is the following one:

```
d=daq("ni");
```

This line code create a *DataAcquisition* object. Then, after the device and its IDs are identified, it's the turn to add the input and output channels to the DataAcquisition object. In particular, the name of the device (*Dev*1 in this case), the name of the channel (*ai* for analog input and *ao* for analog output) and the type of signal that it's intended to assign to that specific channel must be specified in the order. For the analysis two output channels are required since the output is provided in differential mode, and three input channel are required in order to store the actual servo position, the internal command signal and the position error signal.

```
%----------------X AXIS--------------------------
addoutput(d,"Dev1","ao0","Voltage") % x-axis positive signal channel
addoutput(d,"Dev1","ao1","Voltage") % x-axis negative signal channel

addinput(d,"Dev1","ai20","Voltage") % x-axis position
addinput(d,"Dev1","ai21","Voltage") % x-axis internal command signal
addinput(d,"Dev1","ai22","Voltage") % x-axis position error signal

%-----------------Y AXIS-------------------------

addoutput(d,"Dev1","ao2","Voltage") % y-axis positive signal channel
addoutput(d,"Dev1","ao3","Voltage") % y-axis negative signal channel

addinput(d,"Dev1","ai0","Voltage")  % y-axis position
addinput(d,"Dev1","ai1","Voltage")  % y-axis internal command signal
addinput(d,"Dev1","ai2","Voltage")  % y-axis position error signal
```

Finally, reading and writing processes, which can be performed simultaneously via:

```
inputData=readwrite(d,outputData,"OutputFormat","Matrix");
```

where *inputData* is the matrix made up of six colons, in each of which a signal coming from a particular input channel is stored and *outputData* is the matrix containing the differential signals for the four output channels.

### 3.5.3 NI6211

Unfortunately, the NI6343 has only 4 analog output ports. This means another I/O device is needed in order to translate code instructions in voltage signals useful to command the voltage optical attenuator. Indeed, as described in Sec.3.3.5, the V1550A provides an attenuation proportional to the input voltage within the interval $[0, 5]$V. Thus, the NI6211 I/O was introduced in the setup. This time the task consisted of generating a constant signal lasting a couple of seconds necessary to set the desired attenuation level. Since the V1550A is an electromechanical system, once the signal generation ends, the attenuation level remains constant and there is no need for continuous generation in the background. For most of the time a matlab script very similar to the one described above was used it will no be reported in this document.

## 3.6 Balancing the setup

The objective of a SS-OCT is to acquire the beat signal caused by the superposition of the two replicas of the laser pulse, but some device parameters be kept in consideration. First of all the relative delay $\tau$ between the two signals must be less than the source coherent time, then the beat frequency has to fall in the electronic bandwidth of the photodetector and the acquisition device. Assuming a linear frequency swept of the laser, the BPD provides an output current whose frequency is proportional to the optical path difference between the arms of the interferometer:

$$I \propto \cos\left(2\pi\sigma_f \tau t + \theta_0\right) \tag{3.19}$$

and the beat frequency is given by the optical path difference $\Delta z$ as:

$$f = \sigma_f t = \sigma_f \frac{n\Delta z}{c_0} \tag{3.20}$$

where the refractive index $n$ of the optical fiber is assumed to be 1.466 as the entire setup is based on SMF-28 Corning optical fiber family. Since the acquisition device bandwidth is smaller than the one of the detector, this means that the maximum optical path difference must ensure that the beat frequency is within the 250 MHz band. Rearraging the Eq.3.20

the maximum optical path difference is $\Delta z \approx 10$mm. However, even if a beat signal can be shown if this condition is matched, it must be remembered that the maximum clock frequency is $f_{clock,max} \approx 332$ MHz so that the maximum beat frequency that can be digitized without any spatial aliasing artifacts is $f_{clock,max}/2$ according to the Nyquist theorem. For this reason $\Delta z < 7$mm in fiber.

### 3.6.1 Measurement of lengths

To meet this requirement, it's necessary to perform very accurate measurements of the length of each part of the device. For this reason an Optical Frequency-Domain Reflectometer (OFDR) was used, in particular the OBR 4600 by Luna Innovations [28].For simplicity of discussion, only the measurement procedure of a single coupler will be illustrated and in sec.3.6.2 the final measurements of all the parts of the device will also be reported.

Once connected one of the ports of the coupler at the OFDR, the resultant setup is the following one:

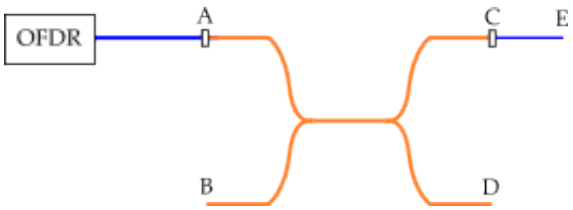


**Figure 3.29:** Measurement scheme on a fiber couple

Since for each input port, the OFDR displays two peaking almost overlapped corresponding to the two output ports, it's necessary to use a patch cord in order to simplify the association between each output port and its own peak on the trace. So for each input port, the procedure is repeated twice connecting the patch cord first to one output port and then to the other. The corresponding trace displayed of the scheme measurement in Fig.3.29 is:

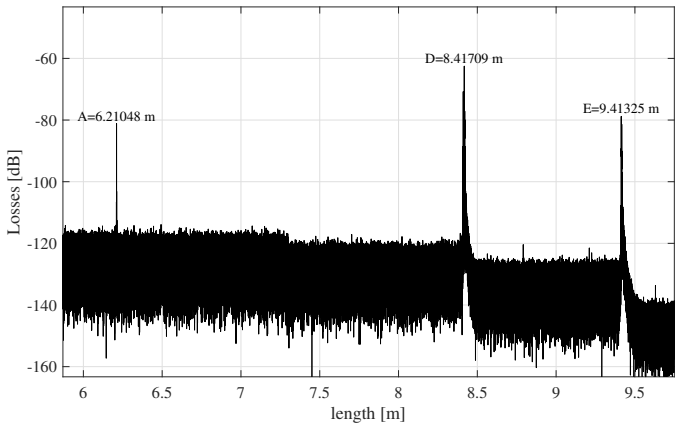


**Figure 3.30:** Example of measurement on a coupler

It can be seen a first peak around 6 m, which is the length of the first patch cord, which connects the OFDR to the coupler, then the peak of the port "D", which is decoupled by port "C" thank to the patch cord long around 1 m which makes the peak "E" appear at 9.41325 m.

### 3.6.2 Final circuit

Putting together all the devices introduced in this chapter, the circuit obtained is the one shown in Fig.3.31. The base, made up of the MaCh-Zehnder interferometer, is easily recognisable, also thanks to the replacement of the reference mirror with an air transmission portion, useful for balancing the setup. In particular, the choice to opt for a transmission air delay is due to the problems that the reflections could cause once part of them were to return to the source. To obtain a similar configuration, two F280AP-C collimators (sec.3.4.1) were mounted on the cage shown in Fig.3.32 using two supports, one fixed (CP02T/M by Thorlabs) and the other equipped with a graduate adjuster knob, capable of moving the collimator up to 2 millimeters along the longitudinal axis (SM1Z by Thorlabs).

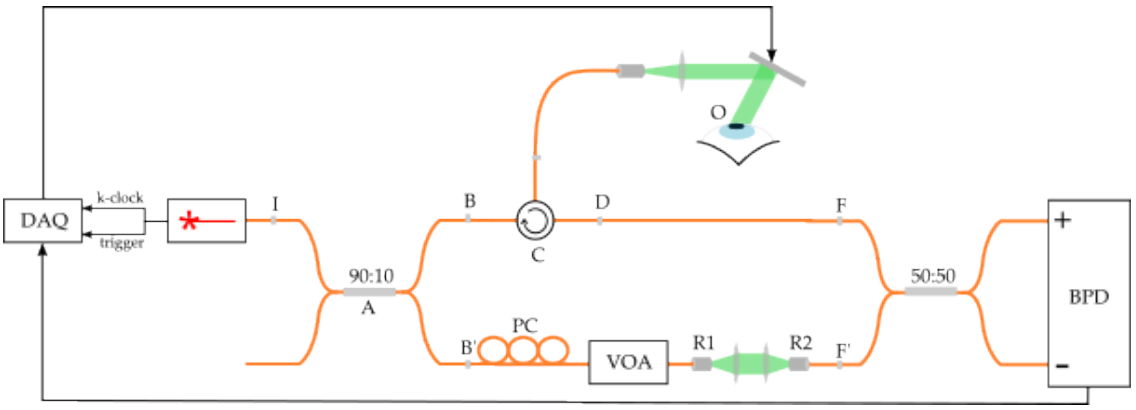


**Figure 3.31:** OCT system

The steps to balance the circuit were as follows:

1. measure the entire reference arm $\overline{IAB'R1}$,where "A" is the centre of the first coupler;
2. measure the first portion of the sample arm $\overline{IABC}$, where "C" is the centre of the circulator;
3. measure the portion $\overline{CO}$, where "O" is the lens focus;
4. measure the distance $\overline{CD}$;
5. build a fiber optic link of suitable length for the $\overline{DF}$ section;
6. adjust the balance moving one of the collimator of the air delay.

The results of the measurements are summarized in the following table:

**Table 3.12:** Length of the device parts

| Section | Length |
|---|---|
| $\overline{IAB'R1}$ | 10.261 m |
| $\overline{IABC}$ | 3.267 m |
| $\overline{CO}$ | 2.245 m |
| $\overline{CD}$ | 1.067 m |
| $\overline{DF}$ | 3.753 m |

The resulting reference arm was 10.557 m long, meanwhile the sample arm was 10.564m, with an unbalance value of 7 mm. In order to adjust this value, the transmission in the air was shortened of the equivalent value in air, i.e. $\approx$ 10 mm.

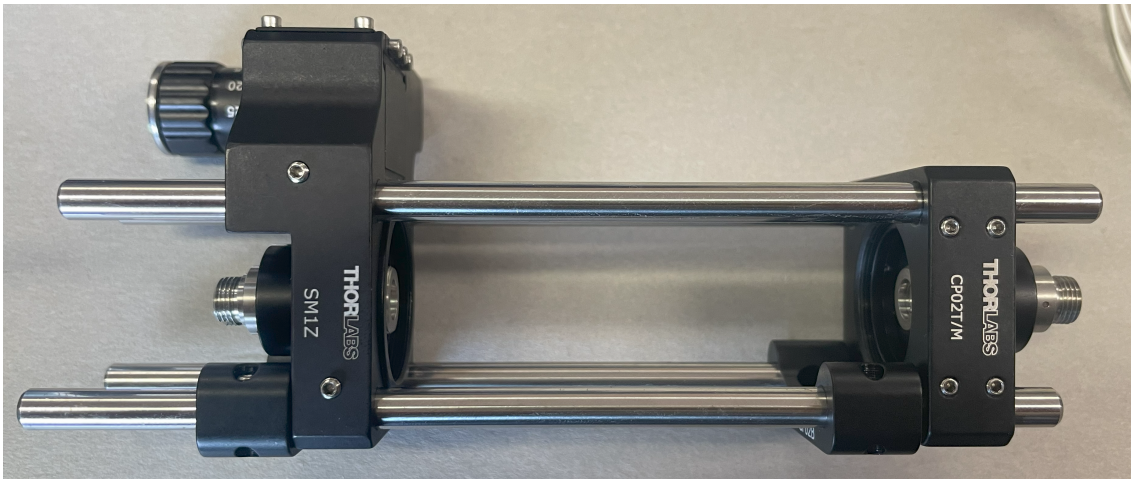


**Figure 3.32:** Air delay mounted in the cage system

# 4 Results

## 4.1 First measures

The first measure taken with the setup had a opaque green square plastic foil whose thickness was 1.8 mm (Fig.4.1). As it can be seen from the its B-scan (Fig.4.2), the image has an high distortion rate. This means that a dispersion mismatcj exists between the two arms of the interferometer.

**Figure 4.1:** Green plastic foil

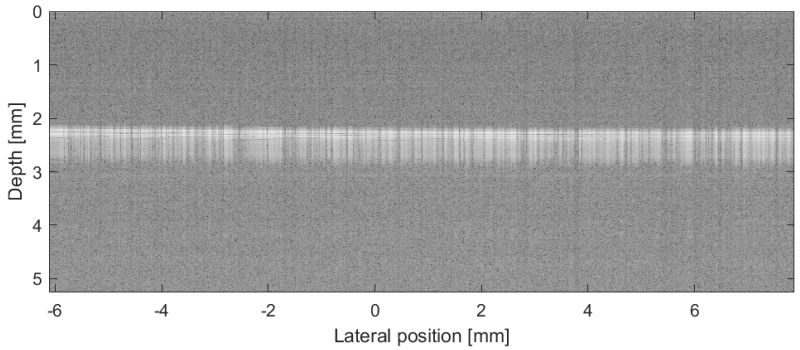


**Figure 4.2:** Green plastic foil first acquisition

## 4.2 Overview of Dispersion Origins

In optical fiber based systems, signal dispersion is a consequence of different factors. Until the dispersion in both of the interferometer arms is comparable, there's no degradation in axial resolution and thus distortions in images are limited, but as the dispersion mismatch grows, the quality of the image becomes poorer due to the degradation of the peak height of the interference envelope, which reduces the system's dynamic range. In particular, dispersion is influenced by:

- intermodal dispersion: in this case, there is no multimodal optical fiber, so this factor is not kept in consideration;
- intramodal dispersion: it consists in the pulse spreading in the single mode optical fiber. It's also called *chromatic dispersion* due the fact that the phase velocity and group velocity of the light propagating in a medium depend on the optical frequency. When talking about lenses, chromatic dispersion is closely linked to the concept of *chromatic aberration*. In fact, chromatic aberration (sec.2.4.3) is nothing more than the effect of chromatic dispersion that characterizes non-achromatic lenses.
- Polarization mode dispersion: since the fiber material is not perfectly uniform, each polarization mode will encounter a slightly different refractive index. As a consequence each mode will travel with a different speed.

As the polarization dispersion is assumed to be already compensated thank to the polarization control, the main attributable causes for dispersion remains chromatic dispersion. In the next sections the characteristics, causes and analyzes carried out on chromatic dispersion will be discussed. Finally, the solutions designed to mitigate its effect within the setup will be presented.

## 4.3 Chromatic dispersion analysis

### 4.3.1 Chromatic dispersion

One of the problems that may come out in OCT devices using broadband laser sources is the chromatic dispersion in optically-dense materials like water, tissue and glass. This phenomena is caused by the dependence of the refractive index on wavelength, so that the different waves travel with different velocities, dispersing the light and in general, the amount of chromatic dispersion is linearly correlated to the length of the dispersive medium.

In OCT systems, quite huge amounts of chromatic dispersion can be tolerated in both the arms of the interferometer only if they are comparable quantities,so that a coherence function without any artifacts can be produced. If one of the arms has more dispersive components, it has much more chromatic dispersion of the other one, and it can be a serious problem in terms of image quality.

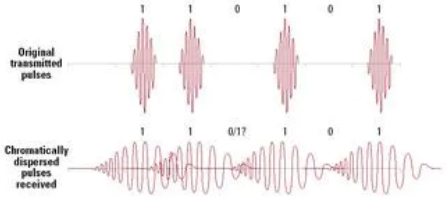


**Figure 4.3:** Chromatic dispersion effects through a dispersive medium

A dispersion mismatch between the arms introduces a phase shift $e^{i\varphi(\omega)} = e^{\beta L}$ in the complex cross spectral density, with L equal to the different paths length. A method to quantify the amount of chromatic dispersion is based on the Taylor expansion of the phase term $\varphi = \beta L$ as function of the angular frequency $\bar{\omega} = \omega - \omega_0$, where $\omega_0$ represents the central angular frequency and $\beta$ the propagation coefficient:

$$\varphi(\bar{\omega}) \approx \varphi_0 + \bar{\omega}\varphi_1|_{\bar{\omega}0} + \frac{1}{2}\bar{\omega}^2\varphi_2|_{\bar{\omega}0} + \frac{1}{6}\bar{\omega}^3\varphi_3|_{\bar{\omega}0} + \gamma \tag{4.1}$$

where the different terms have the following meaning:

- The zero-order term represent a common phase shift;
- The first-order term coincides with the inverse group velocity $\frac{\partial\varphi}{\partial\bar{\omega}}$;
- The second-order terms contains the group delay dispersion $\frac{\partial^2\varphi}{\partial\bar{\omega}^2}$;

- The third-order term contains the third-order dispersion $\frac{\partial^3 \varphi}{\partial \omega^3}$;
- $\gamma$ represents the superior degrees (neglected for the purposes of this thesis).

Dispersion mismatch between the two arms is largely compensated by the second order term, but in some cases, especially when an ultra-broadband source is used, adjustement of higher order dispersion terms can be required.[3]

### 4.3.2 Causes

Since chromatic dispersion is caused by the temporal (and so spatial) spread of the light, in order to quantify this effect, dispersion parameter D evaluation is useful because it gives the variation of the delay per unit variation of the source wavelength and per unit distance of propagation. In particular D is given by:

$$D = \frac{\partial}{\partial \lambda}\left(\frac{\partial \varphi}{\partial \omega}\right) \tag{4.2}$$

As reported in the following subsections, data was collected as function of the wavelength, so making the appropriate algebraic manipulations

$$\frac{\partial}{\partial \lambda}\left(\frac{\partial \varphi}{\partial \omega}\right) = \frac{\partial \omega}{\partial \lambda}\frac{\partial^2 \varphi}{\partial \omega^2} = \frac{\partial \omega}{\partial \lambda}\left[\frac{\partial}{\partial \omega}\left(\frac{\partial \varphi}{\partial \lambda}\frac{\partial \lambda}{\partial \omega}\right)\right] \tag{4.3}$$

and considering that

$$\omega = \frac{2\pi c}{\omega} \tag{4.4}$$

D is finally given by:

$$D = -\frac{\lambda^2}{2\pi c}\frac{\partial^2 \varphi}{\partial \lambda^2} - \frac{\lambda}{\pi c}\frac{\partial \varphi}{\partial \lambda} \tag{4.5}$$

It's also important to quantify the trend of D, which is represented by the parameter S, called "slope":

$$S = \frac{\partial D}{\partial \lambda} \tag{4.6}$$

which can be written as:

$$S = -\frac{\lambda^2}{2\pi c}\frac{\partial^3 \varphi}{\partial \lambda^3} - \frac{2\lambda}{\pi c}\frac{\partial^2 \varphi}{\partial \lambda^2} - \frac{1}{\pi c}\frac{\partial \varphi}{\partial \lambda} \tag{4.7}$$

D is usually measured in $^{ps}/_{nm \times km}$, meanwhile S is usually given in $^{ps}/_{nm^2 \times km}$. In order to investigate what caused so a large amount of chromatic dispersion shown in 4.1, it was necessary to

make a step by step analysis based on a Mach-Zehnder interferometer (Fig.4.4), putting inside the different devices described in Chap.3. In particular, the analysis was focused on the optical fiber,VOA, circulator and on the air delay.

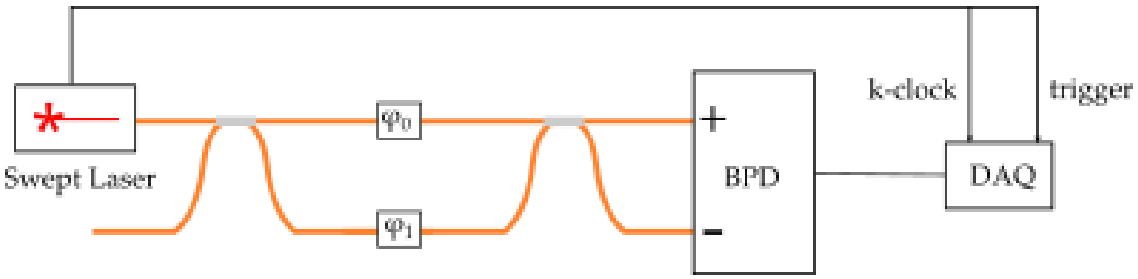


**Figure 4.4:** Setup used in dispersion evaluation

The analysis performed was based on the setup reported in Fig.4.4, where both the arms of the interferometer are supposed to introduce a phase factor$\varphi$. In particular, the designated reference arm produce the phase factor $\varphi_0$, meanwhile the phase factor $\varphi_1$ is introduced by the arm in which the VOA, the circulator and the air delay will be positioned. So the dispersion mismatch phase factor is proportional to the difference $\varphi_1 - \varphi_0$. Once the ATS9350 makes an acquisition, the image obtained is processed through a specific Matlab script provided by the Biophotincs Photonic and Electromagnetic Group Laboratory, with which is possible to extract the phase factor. Once the phase difference is known, thoutgh another Matlab script written based on the Equations 4.5 and 4.7 it's possible to quantify the amount of dispersion mismatch.

#### 4.3.2.1 Fiber

In order to test this approach, the first case taken in consideration is a pure Mach-Zehnder interferometer based only on two fiber couplers. In particular the 90:10 TW1300R2A2 and the 50:50 TW1300RR5A2 used in the OCT designed setup. In this case the expected values can slightly differ from the values in Tab.3.2, but they also must remain comparable to them as the couplers are made up of SMF-28 optical fiber. The image taken from the DAQ is the following one:

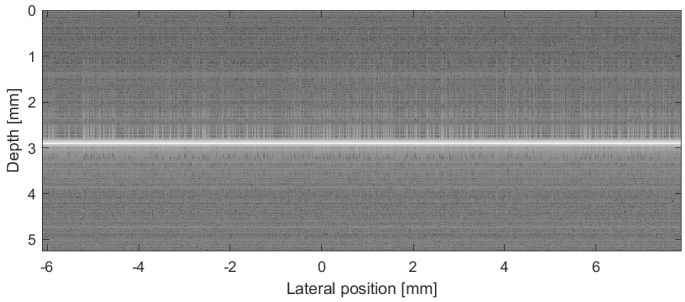


**Figure 4.5:** Image taken by ATS9350 DAQ of the Mach-Zehnder interferometer

The image above shows a very thin line, as sign that the dispersion in this case is very low. Indeed, the corresponding $\varphi$, $D$ and $S$ per unit length parameters have the following trends, whose corresponding average values are $|D_{avg}| = 12 \cdot 10^{-4}$ ps/nm and $|S_{avg}| = 3.8441 \cdot 10^{-6}$ ps/nm$^2$:

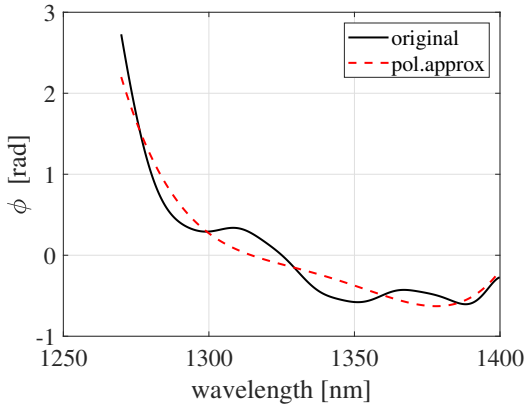


**Figure 4.6:** $\varphi$ factor extracted by the Mach-Zehnder interferometer and the polynomial curve used to approximated it in calculations.

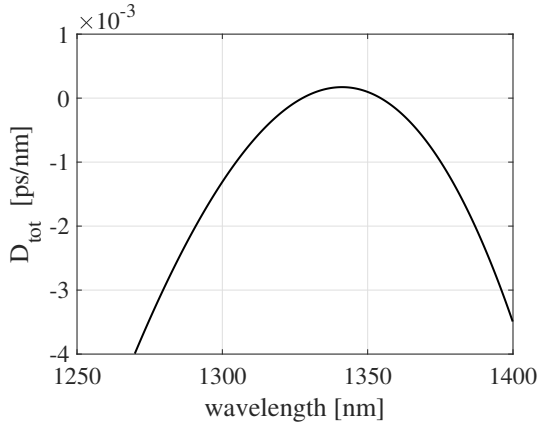


**Figure 4.7:** D parameter of Mach-Zehnder interferometer

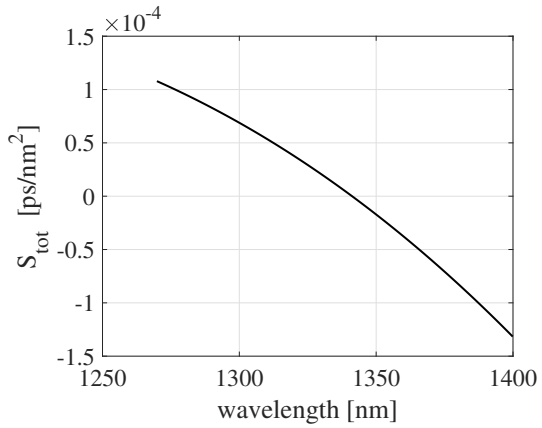


**Figure 4.8:** S parameter of Mach-Zehnder interferometer

These results match the hypothesis according to which SMF-28 family optical fiber produces a very low dispersion, so that the main problems shown in Fig.4.2 don't come from the optical fiber used. As further proof of this statement, let's consider for example an one meter mismatch in between two SMF-28e+ optical fiber paths. Now, let's consider the phase factor $\varphi$ introduced in Eq.4.1 and substitute $L$ with 1 meter. The corresponding step response can be seen as the inverse Fourier transform of the transfer function $H(\bar{\omega}) = e^{j\varphi}$. In order to highlight the quality of this type of fiber, below (Fig.4.9) is reported the step response considering only $\varphi_1 = \beta_1 L$ and then considering also $\varphi_2 = \beta_2 L$. The corresponding spread of the pulse is pratically absent, due to the very low value of the dispersion parameter:

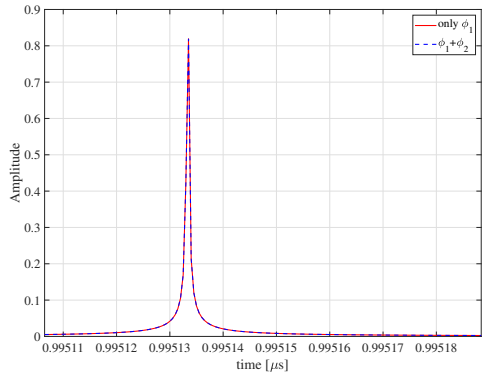


**Figure 4.9:** Impulse response of SMF28e+ with and without considering dispersion parameter

#### 4.3.2.2 Circulator

Since the signal passes through the circulator twice, in this case two separated analysis were performed. The first one regards the passage from port 1 to port 2 , meanwhile the second one regards the passage from port 2 to port 3. Starting from the first case, the image taken with the DAQ by inserting the circulator in the setup of Fig.4.4 is the following one:

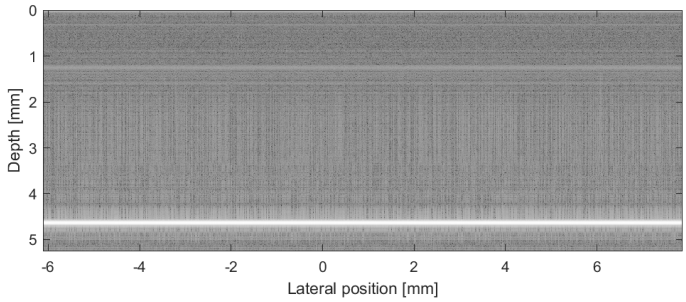


**Figure 4.10:** Image taken by ATS9350 DAQ of the Mach-Zehnder interferometer with circulator(ports 1$\longrightarrow$2)

As it can be seen, also this time the amount of the dispersion seems to be limited, indeed the phase factor $\varphi$ and the dispersion parameters D and S are:

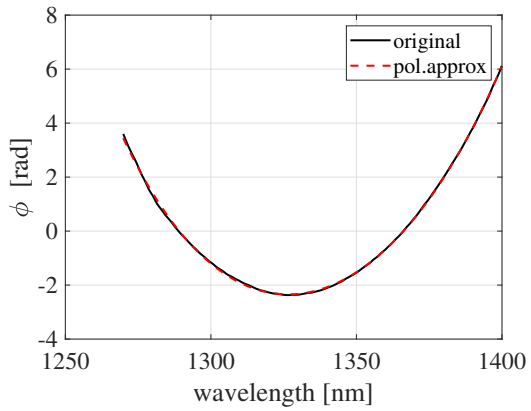


**Figure 4.11:** Phase factor extracted and the polynomial curve used to approximated it in calculations.

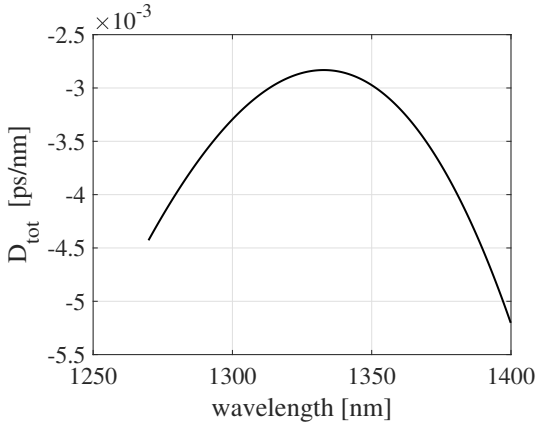


**Figure 4.12:** D parameter of the circulator (ports 1⟶2)

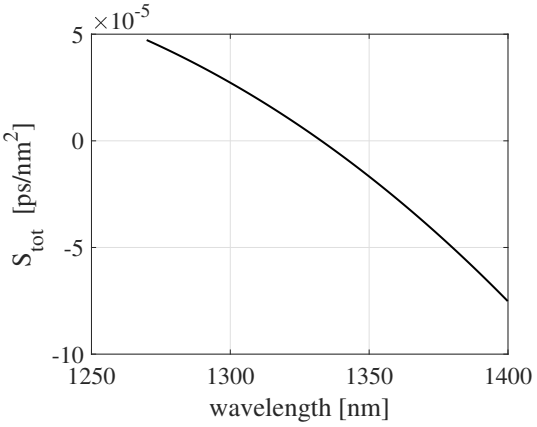


**Figure 4.13:** S parameter of the circulator (ports 1⟶2)

As confirm of the low dispersion introduced from port 1 to port 2 of the circulator, the average values of the parameters are $|D_{avg}| = 35 \cdot 10^{-4}$ ps/nm and $|S_{avg}| = 5.9586 \cdot 10^{-6}$ ps/nm$^2$. Things are totally different regarding the passage from port 2 to port 3. In fact, as can be seen from figure 4.14 and figure 4.15, the dispersion amount is very high.

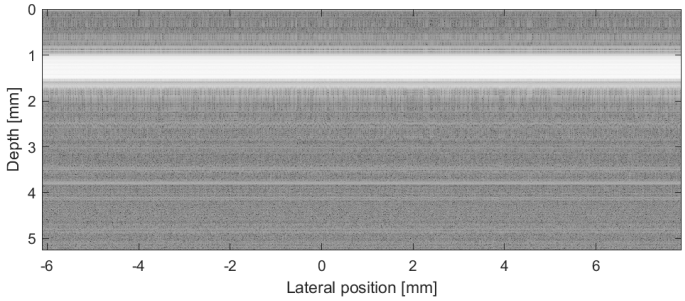


**Figure 4.14:** Image taken by ATS9350 DAQ of the Mach-Zehnder interferometer with circulator(ports 2⟶3)

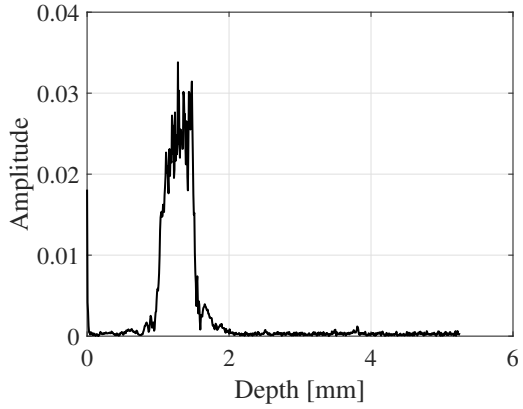


**Figure 4.15:** Spatial spread of the beat signal due to the passage through the ports 2 and 3 of the circulator

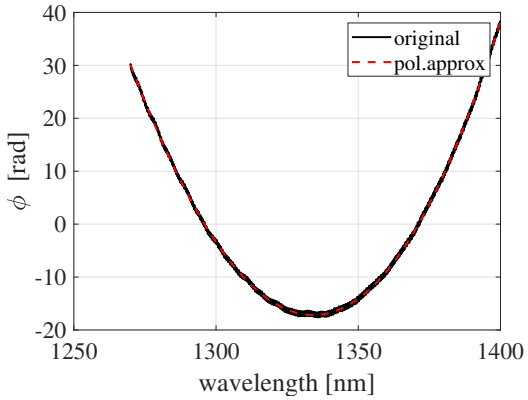


**Figure 4.16:** Phase factor extracted and the polynomial curve used to approximated it in calculations for ports $2 \longrightarrow 3$ in the circulator.

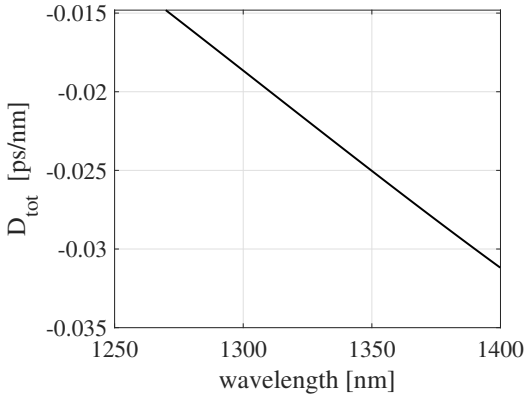


**Figure 4.17:** D parameter of the circulator (ports $2 \longrightarrow 3$)

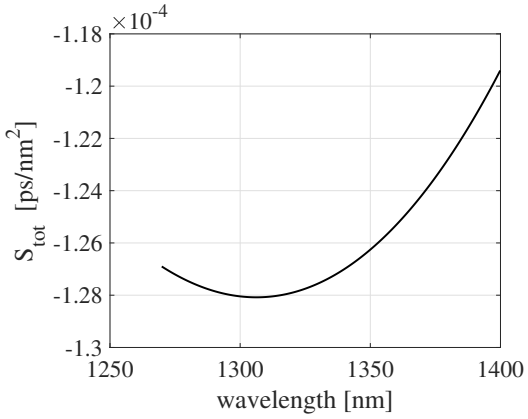


**Figure 4.18:** S parameter of the circulator (ports $2 \longrightarrow 3$)

This time $|D_{avg}| = 231 \cdot 10^{-4}$ ps/nm and $|S_{avg}| = 1.2592 \cdot 10^{-4}$ps/nm$^2$.

#### 4.3.2.3 VOA

Here the results of the analysis on the voltage optical attenuator set to 0 dB level of attenuation are reported.

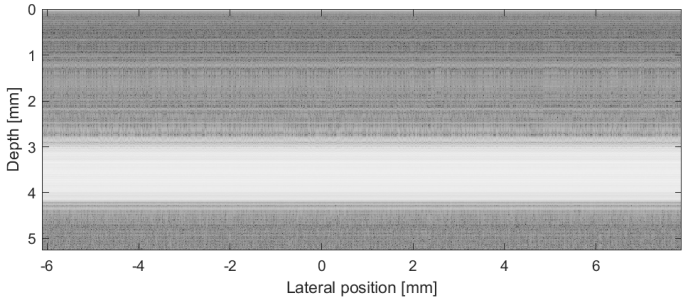


**Figure 4.19:** Image taken by ATS9350 DAQ of the Mach-Zehnder interferometer with VOA inside

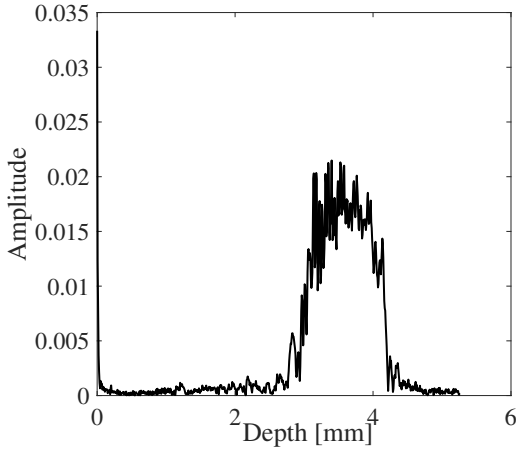


**Figure 4.20:** Spatial spread of the beat signal due to the passage through the VOA

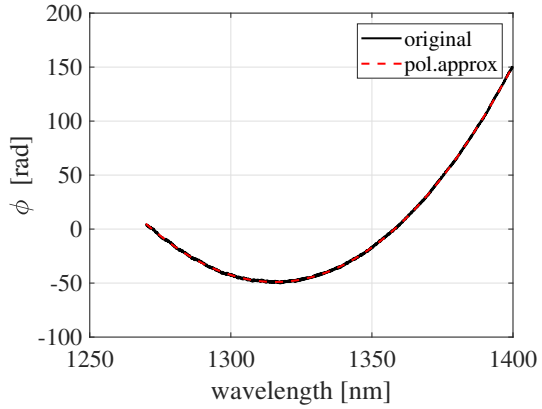


**Figure 4.21:** Phase factor extracted and the polynomial curve used to approximated it in calculations of the VOA behaviour.

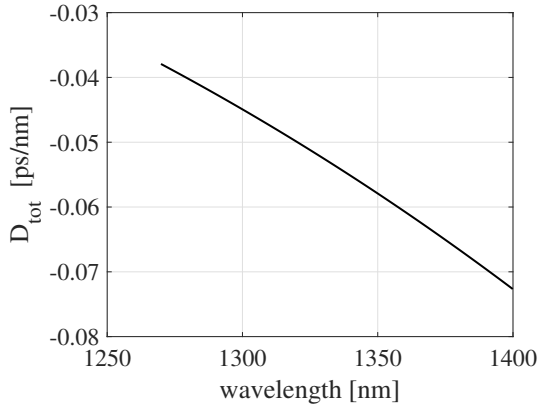


**Figure 4.22:** D parameter VOA

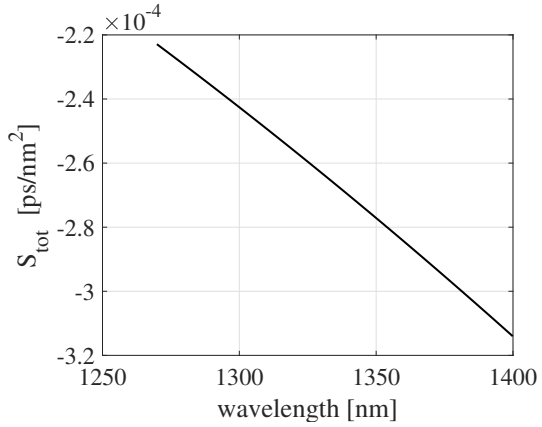


**Figure 4.23:** S parameter VOA

$$|Davg| = 543 \cdot 10^{-4}\text{ps/nm and } |S_{avg}| = 2.6712 \cdot 10^{-4}\text{ps/nm}^2$$

#### 4.3.2.4 Dispersion in collimators

Similarly to what is reported in the previous sections, the results of the analysis on the transmissive air delay are:

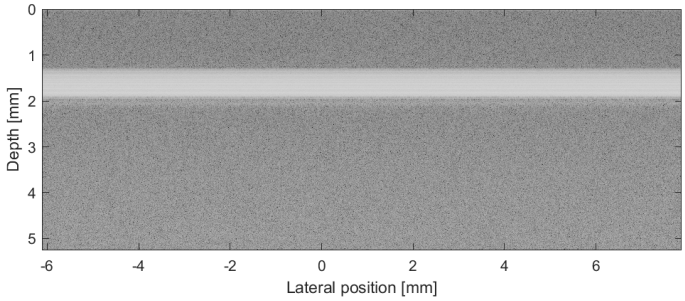


**Figure 4.24:** Image taken by ATS9350 DAQ of the Mach-Zehnder interferometer with air delay

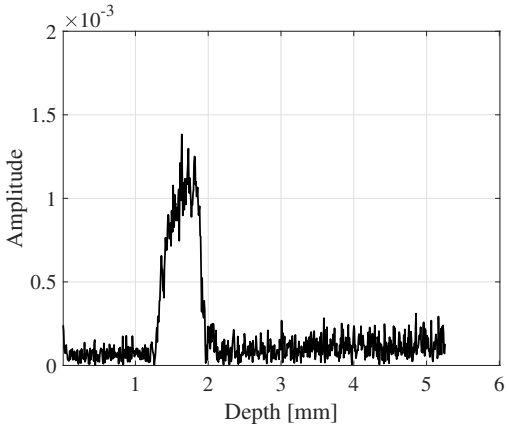


**Figure 4.25:** Spatial spread of the beat signal due to the passage through the air delay

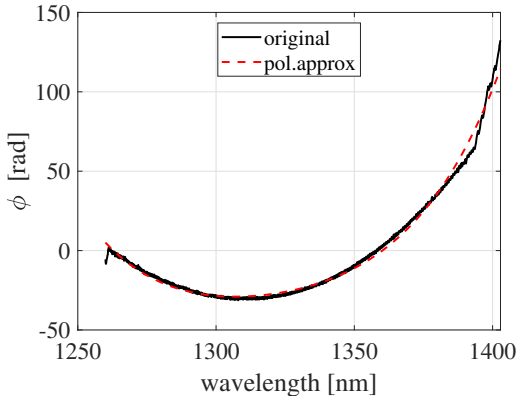


**Figure 4.26:** $\varphi$ factor extracted and the polynomial curve used to approximated it in calculations of the air delay behaviour.

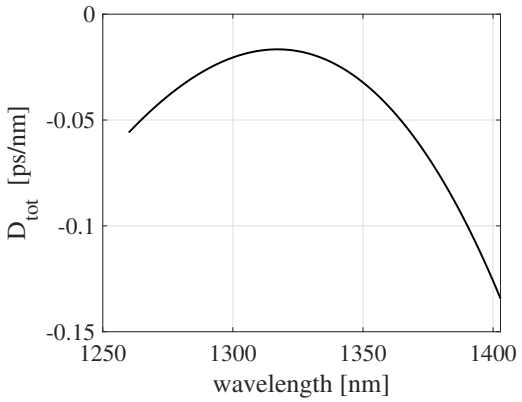


**Figure 4.27:** D parameter of the air delay

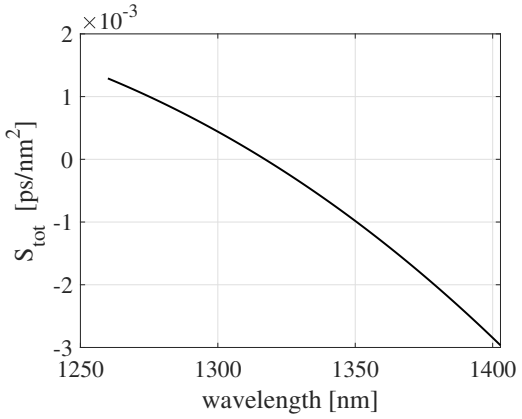


**Figure 4.28:** S parameter of the air delay

$|Davg| = 447 \cdot 10^{-4}$ps/nm and $|S_{avg}| = 5.4903 \cdot 10^{-4}$ps/nm$^2$

## 4.4 Solutions

As shown above, each device introduce a significant dispersion. Considering that the most dispersive devices are placed in the reference arm in the setup of Figure 3.31, a drastic setup change is required to minimize the mismatch. The solution implemented in Figure 4.29 involves moving the VOA from the reference arm to the input port of the first coupler and eliminating the transmissive air delay and replacing it with a reflective one. This solution provides the advantage of having double control over the transmitted power. In fact, in addition to the common control by the VOA, it is possible to have control only on the power of the reference arm via the relative collimator-mirror orientation explained in section 4.4.0.1. In Tab.4.1 the length values for circuit balancing are reported.

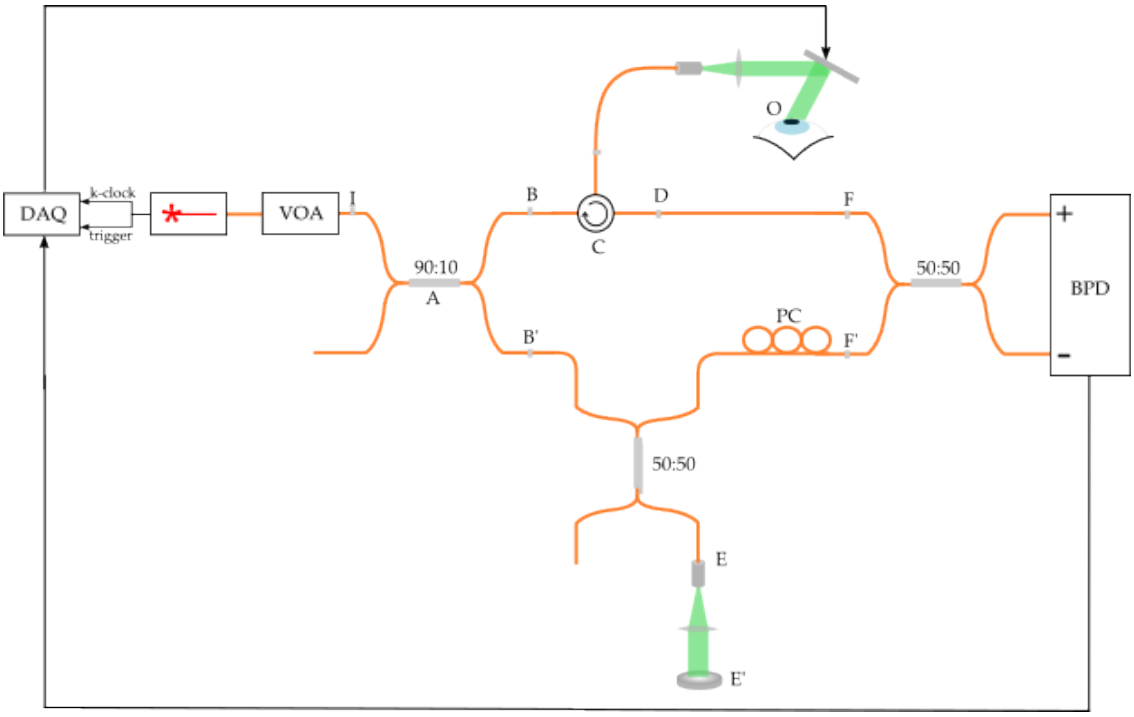


**Figure 4.29:** Solution used to overcome dispersion issues

**Table 4.1:** Length of the device parts

| Section | Length |
|---|---|
| $\overline{IABC}$ | 3.267 m |
| $\overline{CO}$ | 2.245 m |
| $\overline{CDF}$ | 1.067 m |
| $\overline{IAB'E}$ | 5.503 m |
| $\overline{EF}$ | 2.221 m |
| $\overline{EE'}$ | 4.15 cm |

#### 4.4.0.1 Achromatic collimator

The main problem of the F280-APC-C collimator, as already said, is the chromatic aberration. In order to deal with this problem, a system composed of an achromatic doublet was used. In particular, the PAF-X-15-B by Thorlabs shown in Fig.4.30 was used. It's an achromatic fiber port which collimates light over a large wavelength range. Mounted on a cage similar to Fig.3.32, the built-in lens can be aligned with five degrees of freedom, meanwhile in front of it a mirror was positioned,so that the signal can reach the detector. The main advantage of this type of setup, in addition to the lower dispersion, is the fact having five degrees of freedom, so controlling the tilt of the lens, the power reflected by the mirror is also kept under control.

**Figure 4.30:** PAF

#### 4.4.0.2 Numerical compensation

The B-scan of the same green plastic foil of Fig.4.1 taken with the new setup is the following:

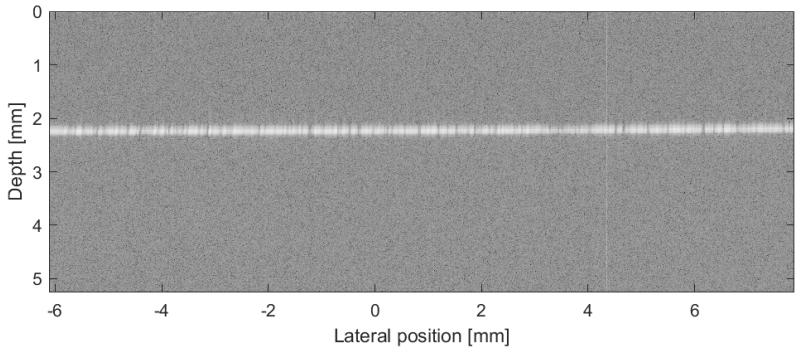


**Figure 4.31:** Green plastic foil second acquisition(not compensated)

It can be seen that this time the distortion rate is much less than before. In order to further improve the image, now it's possible to implement some software compensation strategies:

- Signal windowing:As known from signal theory, performing the FFT of a raw signal can introduce spectral leakage due to discontinuities. To overcome this, it's useful to windowing the time signal before applying the FFT, so that the spectral resolution, and thus in this case the axial resolution, increases.
- Chromatic compensation:To compensate dispersion the method introduced in [29] and [30] was used. Since the dispersion mismatch introduces a phase shift $e^{j\varphi(\lambda)}$ in the complex cross-spectral density, it can be removed by multiplying the dispersed cross-spectral density function by the phase term $e^{-j\varphi(\lambda)}$. To determine the right phase term to use for dispersion compensation it necessary to collect the coherence function from a well reflecting surface. For this purpose, the phase term used to compensate system dispersion is the one taken from the B-scan of the object reported in Fig.4.33.

The Matlab script introduced in sec.4.3.2 gives the possibilities to perform both the corrections. As a raw B-scan is loaded in it, it's possible to apply a window, choosing between Hanning, Hamming and Blackman-Harris windows. Once performed this step, it's possible also perform the dispersion correction loading the phase factor $\varphi(\lambda)$ appropriately chosen.

It's important to highlight the fact that software compensation cannot be done every time there is a large dispersion. Indeed, due to the inevitable detection and amplification noise in the original signal, in case of a large amount of dispersion, the signal value can be comparable to the noise level, so that it can be considered so corrupted that it cannot be recovered numerically. Therefore, compensation must be done phisically at first, and then the software strategies can complete it. For these reasons, the software compensation introduced in this section could not applied after the acquisitions of the first setup.

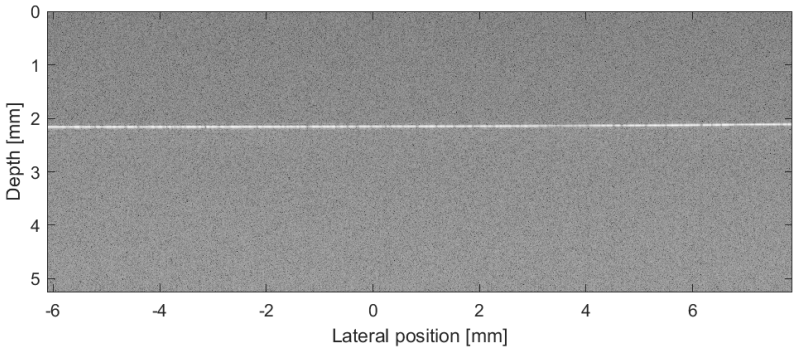


**Figure 4.32:** Green plastic foil second acquisition(compensated)

## 4.5 Final measures

In this section some others B-scan taken with the new setup are reported.

#### 4.5.0.1 Calibrated cylinder with parallel faces

The object shown in Fig.4.33.a had a fundamental role on the software compensation, because it allowed to extract the chromatic dispersion phase term of the system.

**(a)** object used

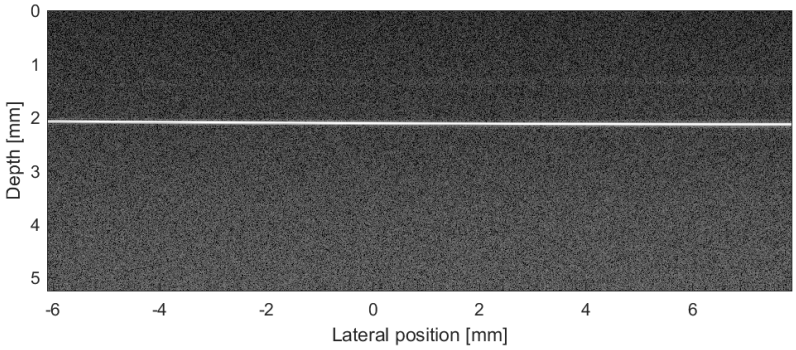


**(b)** B-scan

**Figure 4.33:** OCT image of the object used to extract the phase term for compensation

#### 4.5.0.2 Artificial eye

The artificial eye shown in Fig.4.34.a was used to test the system with a replica of a biological tissue with the advantage of not being able to change over time and therefore providing a reference for the measurements. In particular it provides a very accurate replica of the cornea of a human eye.


**(a)** artificial eye

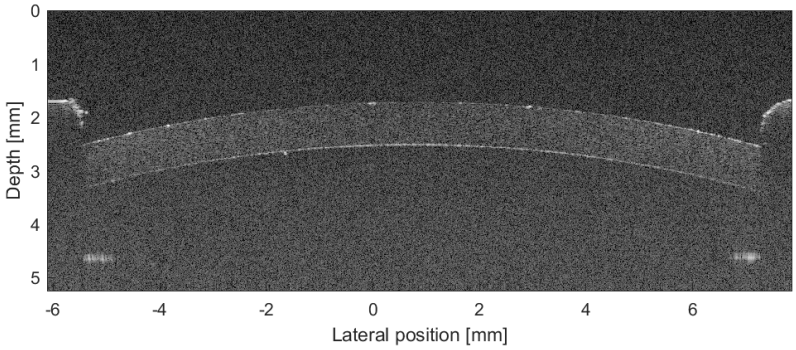


**(b)** B-scan

**Figure 4.34:** OCT image of the artificial eye where the cornea is clearly visible

#### 4.5.0.3 Scotch tape

A very surprising image could be the one shown in Fig.4.35, which portrays the cross section of a roll of scotch tape. From this image it can be appreciated the good axial resolution of the system which allows you to recognize the various layers of rolled tape.

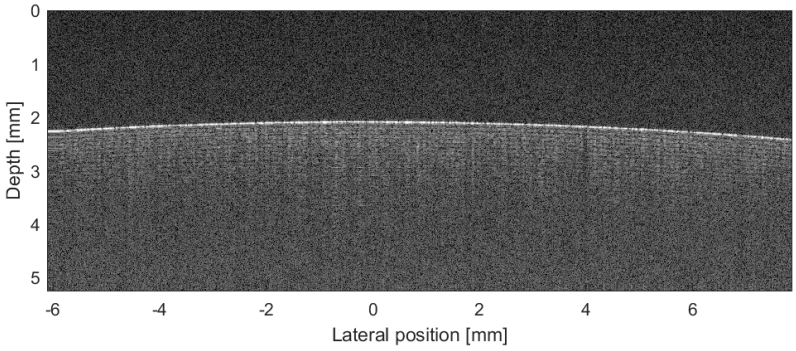


**Figure 4.35:** B-scan of scotch tape

#### 4.5.0.4 Human nail

Considering biological tissues proper, the first acquisition carried out concerned the cross-section of a human nail. In particular in Fig.4.36 it can be seen the nail plate (the outermost surface) and the nail bed in the innermost portion of the image.

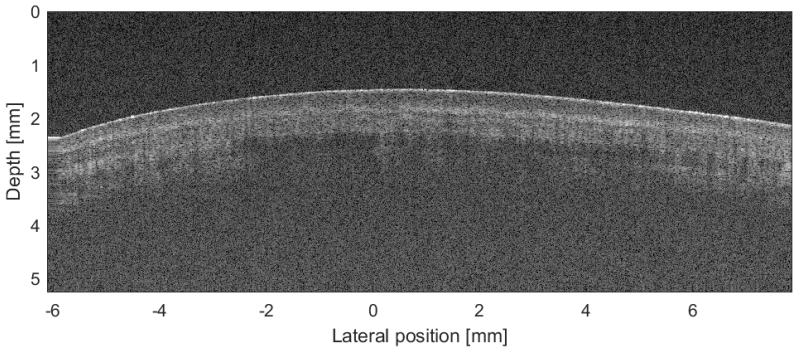


**Figure 4.36:** B-scan of a human nail in vivo

#### 4.5.0.5 Fingertip

Finally, a cross-sectional image of a human fingertip is reported in Fig.4.37, where it can be seen the stratum corneum layer and the stratum basale which divides the epidermis from the dermis.

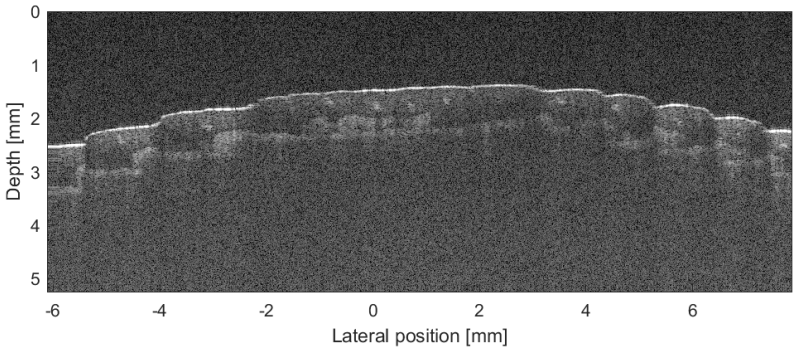


**Figure 4.37:** B-scan of the human fingertip in vivo

# 5 Conclusion

This thesis project continued previous work, investigating the effect of new setups with new devices. In particular, he highlighted how the introduction of optical devices alone is not enough to improve the performance of the setup, but an evaluation of the effects such as dispersion that may occur once the modifications have been made is also necessary. For this reason, during the work presented, a lot of time had to be spent investigating the origin of the problems that led to a notable deterioration in the quality of the images collected. Once the origin was understood, it had to be quantified to have a quantitative vision of the problem.

Thanks to some pre-existing software and others developed during this project, it was possible to find a solution that brought performance back to a level comparable to that of previous thesis works, while implementing a better optical circuit based on a optical circulator.

Future developments will include the evaluation of the insertion of an optical circulator also in the reference arm to completely eliminate possible reflections from the reference arm towards the laser source, or the introduction of achromatic collimators for a transmissive air delay. Furthermore, thanks to the concept of modularity considered in the design of this device, the foundations have been laid for the design of a polarization-sensitive SS-OCT device. Finally, a problem was highlighted linked to the position of the mirrors useful for directing the beam towards the sample, which is why in the future an algorithm will have to be developed that allows compensation, useful for improving the general performance of the device.

# References


[1] M. Wojtkowski, "High-speed optical coherence tomography: basics and applications," vol. 49, no. 16, p. D30. [Online]. Available: https://opg.optica.org/abstract.cfm?URI=ao-49-16-D30

[2] A. A. of Opthalmology. [Online]. Available: https://www.aao.org/

[3] J. Fujimoto and W. Drexler, *Optical Coherence Tomography Technology and Applications*. Springer, 2008.

[4] J. S. Waibel, J. Holmes, H. Hecht, and A. Rudnick, *OCT Image-Guided Treatment of Scars*. Cham: Springer International Publishing, 2020, pp. 83–91. [Online]. Available: https://doi.org/10.1007/978-3-030-29236-2_8

[5] A. Rajabi-Estarabadi, J. M. Bittar, C. Zheng, V. Nascimento, I. Camacho, L. G. Feun, M. Nasiriavanaki, M. Kunz, and K. Nouri, "Optical coherence tomography imaging of melanoma skin cancer," vol. 34, no. 2, pp. 411–420. [Online]. Available: https://doi.org/10.1007/s10103-018-2696-1

[6] S. Geraci', C. Tamburino', and A. L. Manna'. Optical coherence tomography for coronary imaging. Issue: 12 Volume: 9. [Online]. Available: https://www.escardio.org/Journals/E-Journal-of-Cardiology-Practice/Volume-9/Optical-coherence-tomography-for-coronary-imaging , https://www.escardio.org/Journals/E-Journal-of-Cardiology-Practice/Volume-9/Optical-coherence-tomography-for-coronary-imaging

[7] D. Huang, E. A. Swanson, C. P. Lin, J. S. Schuman, W. G. Stinson, W. Chang, M. R. Hee, T. Flotte, K. Gregory, C. A. Puliafito, and J. G. Fujimoto, "Optical coherence tomography," *Science*, vol. 254, no. 5035, p. 1178 – 1181, 1991, cited by: 12667; All Open Access, Green Open Access. [Online]. Available: https://www.scopus.com/inward/record.uri?eid=2-s2.0-0026254046&doi=10.1126%2fscience.1957169&partnerID=40&md5=98ae714591729e8875d17bd38d2a9071

[8] G. Liu, Z. Zhi, and R. Wang, "Digital focusing of OCT images based on scalar diffraction theory and information entropy," vol. 3, pp. 2774–83.

[9] National eye institute | national eye institute. [Online]. Available: https://www.nei.nih.gov/

[10] SS-OCT laser engine. [Online]. Available: https://docs.axsun.com/axsun-technologies-knowledge-base/guides/ss-oct-laser-engine

[11] I. Thorlabs. [Online]. Available: https://www.thorlabs.com/

[12] A. T. Inc. [Online]. Available: https://www.alazartech.com/en/product/ats9350/8/

[13] C. Inc. [Online]. Available: https://www.corning.com/optical-communications/worldwide/en/home/products/fiber/optical-fiber-products/smf-28e-.html

[14] N. I. CORP. [Online]. Available: https://www.ni.com/it-it/support/model.usb-6343.html

[15] A. Silke, D. Sabine, F. Jorg, and M. Frank, *High resolution imaging in microscopy and ophthalmology*. Springer, 2019.

[16] N. I. of Biomedical Imaging and Bioengineering. [Online]. Available: https://www.nibib.nih.gov/science-education/science-topics/optical-imaging

[17] M. Adhi and J. S. Duker, "Optical coherence tomography – current and future applications," vol. 24, no. 3, pp. 213–221. [Online]. Available: https://www.ncbi.nlm.nih.gov/pmc/articles/PMC3758124/

[18] Progetto di un tomografo a coerenza ottica ad alta velocità. [Online]. Available: https://thesis.unipd.it/handle/20.500.12608/25925

[19] G. Marcon, "Design of real-time optical coherence tomography."

[20] G. Keiser, *Optical Fiber Communications*. McGraw-Hill Education, 2010.

[21] A. Fercher, C. Hitzenberger, G. Kamp, and S. El-Zaiat, "Measurement of intraocular distances by backscattering spectral interferometry," *Optics Communications*, vol. 117, no. 1, pp. 43–48, 1995. [Online]. Available: https://www.sciencedirect.com/science/article/pii/0030401895001195

[22] R. P. Encyclopedia. [Online]. Available: https://www.rp-photonics.com/f_number.html

[23] . E. T. Corp. [Online]. Available: https://www.excelitas.com/product-category/axsun

[24] Teledyne LeCroy - WaveSurfer 4024hd. [Online]. Available: https://www.teledynelecroy.com/oscilloscope/oscilloscopemodel.aspx?modelid=11383

[25] A. T. Inc. [Online]. Available: https://www.alazartech.com/en/product/alazardso/26/

[26] High performance balanced photodetector (BPD-1) | insight. [Online]. Available: https://www.sweptlaser.com/content/high-performance-balanced-photodetector-bpd-1-0

[27] NI-DAQmx support from data acquisition toolbox. [Online]. Available: https://it.mathworks.com/hardware-support/nidaqmx.html

[28] Luna OBR 4600 | optical backscatter reflectometer. [Online]. Available: https://lunainc.com/product/obr-4600

[29] B. Cense, N. A. Nassif, T. C. Chen, M. C. Pierce, S.-H. Yun, B. H. Park, B. E. Bouma, G. J. Tearney, and J. F. De Boer, "Ultrahigh-resolution high-speed retinal imaging using spectral-domain optical coherence tomography," vol. 12, no. 11, p. 2435. [Online]. Available: https://opg.optica.org/abstract.cfm?URI=oe-12-11-2435

[30] M. Wojtkowski, V. J. Srinivasan, T. H. Ko, J. G. Fujimoto, A. Kowalczyk, and J. S. Duker, "Ultrahigh-resolution, high-speed, fourier domain optical coherence tomography and methods for dispersion compensation," vol. 12, no. 11, p. 2404. [Online]. Available: https://opg.optica.org/abstract.cfm?URI=oe-12-11-2404

# Acknowledgments

Innanzitutto desidero ringraziare il professor Palmieri per l'opportunità avuta di lavorare a questo progetto, per i suoi consigli e per gli strumenti forniti, i quali hanno alleggerito il mio lavoro.

Un pensiero speciale va ai miei vecchi compagni di corso, su tutti Giovanni e Gloria, con cui ho condiviso i migliori momenti del mio percorso universitario, nonché a Marco per gli innumerevoli aiuti che mi ha dato negli ultimi due anni. Vorrei inoltre ringraziare ogni altra persona incrociata nel mio percorso e che abbia dato anche il più piccolo contributo affinché io potessi arrivare a scrivere questi ringraziamenti.

Vorrei citare anche Riccardo, per le ore di pausa caffè spese a parlare di ogni nostra preoccupazione e per il sostegno che ha saputo darmi durante questo percorso.

Ringrazio Maila, la persona che più di ogni altra ha condiviso con me momenti belli e momenti bui, i cui consigli si sono sempre rivelati un aiuto prezioso e che mi ha saputo trasmettere la sua immensa forza.

Infine, ringrazio di cuore la mia famiglia per il ruolo fondamentale che ha avuto nella mia vita fino ad ora. Grazie Raffaele, Chiara e Sara.